

AD-A198 867

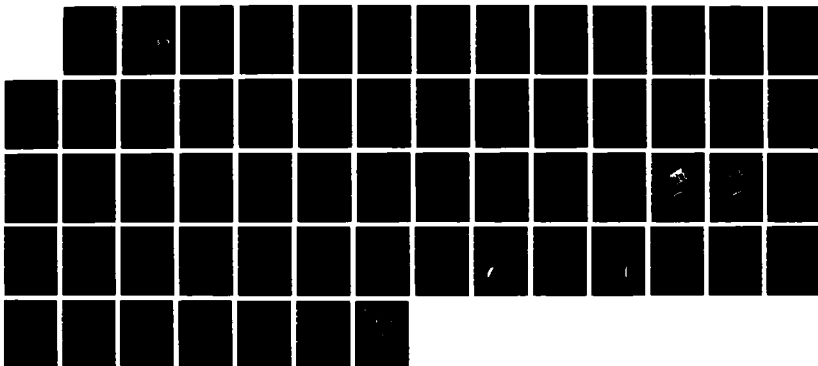
FOG RAIN AND AEROSOL ATTENUATION IN THE ATMOSPHERE(U)
STATE UNIV OF NEW YORK AT ALBANY ATMOSPHERIC SCIENCES
RESEARCH CENTER G G LALA ET AL. 31 DEC 87
ARO-21143.1-G5 DAAG29-84-K-8858

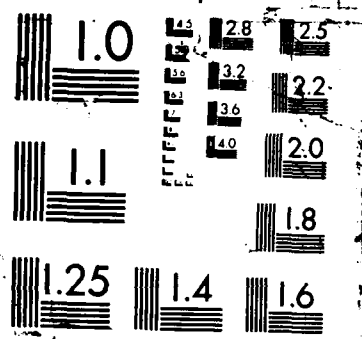
1/1

UNCLASSIFIED

F/G 4/2

NL





AD-A190 867

2

| REPORT DOCUMENTATION PAGE | | READ INSTRUCTIONS BEFORE COMPLETING FORM |
|--|-------------------------------------|--|
| 1. REPORT NUMBER ARO 21143.1-65 | 2. GOVT ACCESSION NO. N/A | 3. RECIPIENT'S CATALOG NUMBER N/A |
| 4. TITLE (and Subtitle) Fog, Rain and Aerosol Attenuation in the Atmosphere | | 5. TYPE OF REPORT & PERIOD COVERED 1 April 1984 to 31 August 1987 |
| 7. AUTHOR(s) G. Garland Lala David R. Fitzjarrald Michael B. Meyer | | 6. PERFORMING ORG. REPORT NUMBER DAAG29-84-K-0050 |
| 9. PERFORMING ORGANIZATION NAME AND ADDRESS Atmospheric Sciences Research Center State University of New York at Albany 1400 Washington Avenue, Albany, NY 12222 | | 10. CONTRACT OR GRANT NUMBER(s) Army Research Office DAAG2984K0050 |
| 11. CONTROLLING OFFICE NAME AND ADDRESS U.S. Army Research Office Post Office Box 12211 Research Triangle Park, NC 27704 | | 12. PROGRAM ELEMENT, PROJECT, TASK AREA & WORK UNIT NUMBERS |
| 14. MONITORING AGENCY NAME & ADDRESS (if different from Controlling Office) | | 13. REPORT DATE December 31, 1987 |
| | | 15. SECURITY CLASS. (of this report) |
| | | 15a. DECLASSIFICATION/DOWNGRADING SCHEDULE |
| 16. DISTRIBUTION STATEMENT (of this Report) Approved for public release; distribution unlimited. | | |
| 17. DISTRIBUTION STATEMENT (of the abstract entered in Block 20, if different from Report) DTIC ELECTE FEB 03 1988 S & D | | |
| 18. SUPPLEMENTARY NOTES THE VIEW, OPINIONS, AND/OR FINDINGS CONTAINED IN THIS REPORT ARE THOSE OF THE AUTHOR(S) AND SHOULD NOT BE CONSIDERED AS AN OFFICIAL DEPARTMENT OF THE ARMY POSITION. NO WARRANTY OF DECISION, UNLESS SO SPECIFICALLY STATED, IS MADE BY THE ARMY. | | |
| 19. KEY WORDS (Continue on reverse side if necessary and identify by block number) Fog Fog Forecasting Fog Evolution Extinction Boundary Layer Liquid Water Content Infrared Extinction Droplet Spectra Radiation Fog Visual Range Aerosols | | |
| 20. ABSTRACT (Continue on reverse side if necessary and identify by block number) Results of a program of data analysis and field measurement of fog formation and fog characteristics are reported. Large scale meteorological influences as well as local fog climatology have been investigated and a simple model based on standard weather observations has been formulated to explain the seasonal trends in fog occurrence. In addition, detailed studies of surface layer and boundary layer structure during fog events are summarized. The importance of initial conditions in determining the potential for fog | | |

formation are discussed. The roles of long wave radiational cooling and turbulent transport in promoting fog formation in each of these regions has been investigated. In many cases, radiational cooling is the dominant mechanism responsible for bringing a deep layer to saturation. Local winds, such as the channeled flow in the Hudson valley, may act either to promote or to prevent fog formation. From this analysis, it is clear that standard surface and upper air observations alone are inadequate inputs for fog forecasting, but must be augmented with more detailed boundary layer observations.

Continuous samples of droplet spectra in fog obtained with a forward scattering droplet spectrometer have been analyzed to investigate the shape of the size distribution as a function of time. Over periods of time of the order of hours, the large drop spectra maintains a similar shape which is well described by the lognormal distribution function. Analysis of the spectra in terms of the distribution parameters indicates that shallow fog distributions are narrower and have smaller mass median diameters than deep fogs. Fogs which begin as shallow fogs and subsequently develop through a deep layer show a corresponding change in the distribution shape toward greater width but smaller mass median diameters.

Analysis of extinction measurements made with forward scatter visibility meters and extinction calculated from fog drop spectra revealed the difficulty in determining the visibility in fog with a single measurement. At high visibility, errors in the calculated extinction are large while at low visibilities the angular truncation error of the forward scatter meter become dominant. Thus it seems that complementary measurements of this type are needed and both measurements themselves need to be improved.

| | |
|--------------------|-------------------------------------|
| Accession For | |
| NTIS CRA&I | <input checked="" type="checkbox"/> |
| DTIC TAB | <input type="checkbox"/> |
| Unannounced | <input type="checkbox"/> |
| Justification | |
| By | |
| Distribution/ | |
| Availability Codes | |
| Dist | Avail and/or Special |
| A-1 | |



88 1 29 032

Fog, Rain, and Aerosol Attenuation in the Atmosphere
Final Report

G. Garland Lala
David R. Fitzjarrald
Michael B. Meyer

December 31, 1987

United States Army Research Office
Contract No: DAAG-29-84-~~D~~-0050

K

Atmospheric Sciences Research Center
State University of New York at Albany
1400 Washington Avenue
Albany, New York 12222

Approved for public release
Distribution unlimited

THE VIEW, OPINIONS, AND/OR FINDINGS CONTAINED IN THIS REPORT ARE THOSE OF THE AUTHOR(S) AND SHOULD NOT BE CONSTRUED AS AN OFFICIAL DEPARTMENT OF THE ARMY POSITION, POLICY, OR DECISION, UNLESS SO DESIGNATED BY OTHER DOCUMENTATION.

Table of Contents

| | |
|---|----|
| Table of Contents | i |
| List of Figures | ii |
| List of Tables | iv |
| 1.0 Introduction | 1 |
| 2.0 Climatology of Albany Radiation Fog | 3 |
| 2.1 Introduction | 3 |
| 2.2 Data base and procedure | 3 |
| 2.3 Radiation fog season | 5 |
| 2.3.1 Identification | 5 |
| 2.3.2 Physical model | 6 |
| 2.4 Synoptic patterns | 7 |
| 2.5 Diurnal characteristics | 11 |
| 2.6 Implications for fog forecasting | 12 |
| 3.0 Hudson Valley Fog Environments | 18 |
| 3.1 Introduction | 18 |
| 3.2 Conceptual models | 19 |
| 3.2.1 Approach to saturation | 19 |
| 3.2.2 Boundary layer model | 20 |
| 3.2.3 Surface layer model | 22 |
| 3.2.4 Local wind model | 23 |
| 3.3. Some conclusions | 24 |
| 4.0 Observations of Droplet Spectra in Radiation Fog | 25 |
| 4.1 Introduction | 25 |
| 4.2 Evolution of drop spectra during dense fog | 26 |
| 4.3 Models of Fog Drop Spectra | 26 |
| 5.0 Optical Extinction Measurements in Radiation Haze and Fog | 33 |
| 5.1 Introduction | 33 |
| 5.2 Data Sources and Instrumentation | 34 |
| 5.3 Instrument Performance | 35 |
| 5.3.1 FSSP-100 | 35 |
| 5.3.2 AEG-MS04 | 36 |
| 5.4 Results | 37 |
| 5.4.1 Extinction ratio | 37 |
| 5.4.2 Extinction-size spectrum | 38 |
| 5.4.2.1 Visual range categories | 39 |
| 5.4.2.2 Temperature categories | 39 |
| 6.0 Summary | 46 |
| 7.0 References | 48 |
| 8.0 Publication Summary | 51 |
| 9.0 Scientific Personnel | 52 |

List of Figures

| <u>Figure #</u> | | <u>Page #</u> |
|------------------|---|---------------|
| Figure 2.1. | Monthly frequency of radiation fog characteristics at Albany, New York, averaged over the period 1970-1979. TOP: Number of events per year; MIDDLE: Fraction of all fogs which are radiation fogs; BOTTOM: Number of hours of fog per each fog event. | 13 |
| Figure 2.2. | Physical model describing the observed radiation fog monthly frequency (+s) at Albany, New York averaged over the period 1970-1979. SOLID: Model fit to the fog frequency using Eq. (2.2). Multivariate least-squares regression yields $a_0=0.089$, $a_1=0.013$, $a_2=0.0052$, and $a_3=0.052$. DASHED: Cooling available. DASH-DOTTED: Cooling necessary. | 14 |
| Figure 2.3. | Surface synoptic patterns associated with radiation fog. | 15 |
| Figure 2.4. | Normalized frequency of hourly radiation fog observations at Albany, New York averaged over the period 1970-1979. | 16 |
| Figure 2.5. | Observations of radiation fog (solid line) as given in Fig. 2.4, but now plotted relative to sunrise time. Also shown are the time of fog development (dashed line) and fog dissipation (dotted line) relative to sunrise time. | 17 |
| Figure 4.1(a,b). | Fog drop number distributions versus time during periods of dense fog on a) 25,26 Sept. 1982, b) 30 Sept - 1 Oct 1982. | 30 |
| Figure 4.2(a,b). | Normalized fog drop mass distribution versus time during periods of dense fog on a) 25,26 Sept. 1982, b) 30 Sept - 1 Oct 1982. | 31 |
| Figure 4.3(a,b). | Drop spectra as measured and derived from a lognormal function fit versus time during periods of dense fog on a) 25,26 Sept. 1982, b) 30 Sept - 1 Oct 1982. Bottom to top respectively, 1) solid - mass median diameter; dotted - 5% and 95% limits of distribution. 2) geometric standard deviation. 3) number concentration: solid - measured; dotted - derived from curve fit. 4) liquid water content: solid - measured; dotted - derived from curve fit. | 32 |
| Figure 5.1. | Angular truncation factor versus particle diameter for an angular range of 10-120 degrees, wavelength of $0.55 \mu\text{m}$, and real index of refraction equal to 1.33. | 41 |
| Figure 5.2. | Ratio of measure extinction (AEG) to calculated extinction (FSSP) versus liquid water content (FSSP). | 42 |

| | | |
|-------------|---|----|
| Figure 5.3. | Mean diameter of the drop-size distribution versus liquid water content. Both quantities calculated from FSSP data. | 44 |
| Figure 5.4. | Average fog extinction-size spectra for visual range categories A) 0.0-0.1 km (solid), B) 0.1-0.4 km (dot-dash), C) 0.4-1.0 km (dash), and D) 1.0-2.0 km (dot). These curves have been normalized by the total integrated extinction coefficient and represent the frequency of extinction per micron interval. | 45 |
| Figure 5.5. | Average fog extinction-size spectra for temperature categories 1) $T \leq 0$ C (solid), and 2) $T > 0$ C (dash). These curves have been normalized by the total integrated extinction coefficient and represent the frequency of extinction per micron interval. | 46 |

List of Tables

| <u>Table #</u> | | <u>Page #</u> |
|----------------|---|---------------|
| Table 2.1. | Monthly distribution of heavy radiation fog events by synoptic type (1970-1979) | 8 |
| Table 2.2. | Surface high pressure center (Type 1) or major ridge axis (Type 2) location relative to Albany, New York | 8 |
| Table 2.3. | Averaged characteristics of heavy radiation fog events by synoptic type, 1979-1970, Albany, New York | 10 |
| Table 2.4 | Percentage of heavy radiation fog events following measurable precipitation, 1970-1979, Albany, New York | 11 |
| Table 5.1 | Least squares curve fits [power law: $Y = A X^B$] for extinction ratio [AEG/FSSP] versus liquid water content graphs. R is the correlation coefficient, N is the number of observations. | 43 |

Fog, Rain, and Aerosol Attenuation in the Atmosphere
Final Report on Contract No: DAAG-29-84-K-0050

G. Garland Lala, David R. Fitzjarrald, and Michael B. Meyer

Atmospheric Sciences Research Center
State University of New York at Albany
Albany, New York 12222

1.0 Introduction

The objectives of this study were: to arrive at a better understanding of the formation of fog, to characterize the microphysics of fog and its role in the extinction of radiation, and to explore other environments characterized by critical levels of optical extinction. The study of fogs was based on the large body of data obtained from the field projects conducted at Albany, New York in 1981 and 1982 (Meyer et al., 1986). This large data set was augmented by other information gathered in a small field project in 1985, which was designed to address new topics related to the fog problem. Included in this data set were other measurements of rainfall characteristics as well as aerosol properties. Because of the large volume of data treated and extensive data analysis that this required, only the most significant results will be reported here.

The analysis of the conditions leading to the formation of fog has included an extended analysis of the synoptic scale features associated with fog formation as well as an attempt to explain the climatological variability of fog observed at Albany, New York. These results provide a basis for improved fog forecasting using standard weather observations.

Detailed analysis of boundary layer and surface layer data has led to an increased understanding of the role of initial conditions in fog formation as well as a better appreciation of the roles of long wave radiation, turbulence, local winds and other processes responsible for bringing the atmosphere to the saturated conditions required for fog formation. These results clearly demonstrate the role of local processes in fog formation and provide guidance for future field investigations.

A large number of droplet spectra were collected in fog during the field experiments posing new challenges for data analysis. New methods for displaying the data as well as analyzing the results have been developed. This effort has led to the realization that fog drop spectra maintain a nearly constant shape over periods of hours while the liquid water content may vary by an order of magnitude. Definite transitions in the drop spectra parameters are associated with fog thickness and boundary layer stability. Implications of

these observations for the modeling parameterization of fog processes and other applications have been addressed.

The problem of the measurement of optical extinction in fog, along with determination of extinction from droplet spectra proved to be challenging. Measurement limitations in both the forward scatter visibility instruments and the droplet spectrometers led to an in-depth investigation of the accuracy of these measurements. As a result of this analysis, it was learned that no one instrument is adequate over the range of visibilities encountered in fog events. Further, the limitations of the techniques are dependent on the nature of the aerosol and the fog drop size distribution. Directions for future research efforts have resulted from this study.

The major results of these studies are presented in the following sections. Details of the analysis, as well as complete presentation of results will be reported in publications being prepared for professional journals.

2.0 Climatology of Albany Radiation Fog

2.1 Introduction

The accurate forecasting of fog events is a discipline which requires an intimate familiarity with local meteorology and fog climatology. Some attention has been given to the identification and geographical distribution of dominant fog types (e.g. radiation, advection, frontal) within the contiguous United States (Stone, 1936; George, 1940; Willett, 1944; Byers, 1959). The most recent presentations of fog frequency distributions over the United States (Court and Gerston, 1966; Peace, 1969; Hardwick, 1973) have delineated general large-scale fog trends. Little information which details regional fog climatologies by fog type exists in the literature.

Average microphysical properties of major fog types have been reviewed by Jiusto (1981). Depending on the fog type present, fog droplets can range in size from 5 to 65 μm diameter, fog thickness can vary from very shallow to over 300 meters, while microphysical properties such as liquid water content and visibility can each differ by factors of two or more. Unique differences in the structure among these fog types suggest that the impact on fog sensitive systems and industries could be quite variable, depending on the fog type present. An increased understanding of local climatological parameters associated with a specific fog type appears to carry some benefit. This would allow better recognition (and presumably more accurate forecasting) of the situations more suitable for certain fog types to occur.

In support of an ongoing field program to study radiation fog mechanisms at Albany, New York (Meyer et al., 1986), a detailed investigation of the local radiation fog climatology was undertaken. The results, with particular emphasis on fog season identification, synoptic patterns, diurnal characteristics and implications for forecasting, are presented here.

2.2 Data base and procedure

The ten year period of 1970 to 1979 was selected for compiling a local fog climatology for Albany. The Local Climatological Data (LCD) monthly summaries, surface weather observation (SWO) forms MF1-10A and MF1-10B, and the North American surface weather maps available from the National Climatic Data Center, National Oceanic and Atmospheric Administration, were used as the primary data base. The LCD's and SWO's were collected for the National Weather Service (NWS) site at the Albany County Airport.

By surveying the LCD's for the decade, an initial data set of 215 "heavy" fog days was assembled. Heavy fog is defined as fog with visibility one-quarter mile or less and is indicated on the LCD as weather type 2 under the column heading "Weather Types on Dates of Occurrence". For the remainder of the text the term "fog" will imply "heavy fog". Next, using the SWO's, a distinction was drawn between a fog day and a fog event. Once the visibility fell to the fog threshold, a fog event was considered to be in progress. Criteria for determining the end of the fog event were: 1) visibility greater than or equal to one mile for twelve or more hours, or 2) visibility greater than or equal to two miles for six or more hours. Thus, it is possible for a fog event to encompass one or more periods of fog and span more than one day. The fog frequency studies of Court and Gerston (1966), Peace (1969), and Hardwick (1973) all utilized the fog day. The use here of the fog event instead of the fog day reduces the data base by 6.5 percent (201 cases). The event approach to describing the local fog climatology, albeit more time consuming, provides a more realistic view since synoptic phenomena are not constrained by the midnight time boundary.

The SWO's were also used to determine fog intensity and record concurrent synoptic conditions. Both hourly (record) and special observations were used. A relative assessment of fog intensity is constructed from the total hours of fog, minimum visibility and the extent of visibility degradation to at least one-sixteenth of a mile. In order to determine fog duration in minutes, measurements at the time of observation were assumed unchanged until the time of the next observation. For each fog event the surface temperature and pressure, resultant and average winds, current and prior precipitation, and snow cover were logged.

The next step was to determine which fog events were of the radiation type. Radiation fog formation depends upon a critical balance between nocturnal long wave radiational cooling and the turbulent diffusion of heat and moisture in the surface layer. Taylor (1917) was perhaps the first to recognize this physical foundation for radiation fog development. Willett (1928), utilizing Taylor's concept, postulated that some dynamic turbulence helped extend the ground cooling (produced by radiational cooling) into the surface layer, while still preserving the surface temperature inversion. Later, Emmons and Montgomery (1947) recognized that cooling by radiative flux divergence in the air itself must also be included in the fog formation theory. Thus, meteorological conditions favorable for the onset of radiation fog must necessarily include thinning, clearing, or absence of cloud cover, minimal wind speed, and falling air temperature due to nocturnal radiational cooling. The presence of cloud cover acts to inhibit the cooling necessary to saturate the air, while excessive wind speed promotes drying of the air and reduces the

cooling rate of the surface layer. However, a completely calm condition (little turbulence) tends to promote dew formation only.

George (1951) cites restricted heating and air-drainage as two primary scenarios favorable for radiation fog. The restricted heating fog scenario assumes that the local air has been under a cloud cover (with or without precipitation) during the day previous to its formation, whereas the air-drainage fog arises from cool air collecting in valleys, such as river valleys. Utilizing these guidelines, along with the SWO's, a clear distinction can be drawn between radiation (143 cases) and non-radiation (58 cases) fog.

Finally, the appropriate North American surface maps were used to determine which synoptic patterns prevailed during the radiation fog events.

2.3 Radiation fog season

2.3.1 Identification

Fig. 2.1a shows the monthly frequency of radiation fog events per year averaged over the ten year observation period at Albany. There were a total of 143 radiation fog events during this time span. A distinct autumnal "radiation fog season" is apparent, with more than half of the fog events concentrated in the months of September and October. By season, radiation fogs are most prevalent in the autumn (September, October, November) with 65.0% of the total, followed by summer (June, July, August -- 23.8%), spring (March, April, May -- 8.4%) and wintertime (December, January, February -- 2.8%). The observed October maximum agrees well with the published data of Stone (1936) for Northeastern valley fogs.

71% of all fog events at Albany can be classified as radiation fogs. The ratio of radiation fog events to all fog-type events is plotted versus month in Fig. 2.1b. It should be noted that there is an autumnal peak in radiation fog percentage, with nearly all fogs in September and October being of the radiation type. This peak, however, is much broader than that of Fig. 2.1a. During the winter and early spring radiation fogs are relatively rare (13.2%). A gradual increase in percentage is indicated following March, with well over 80% of all fog events being radiation-type during the months of June through October.

One measure of the radiation fog intensity is given by the monthly frequency of the fog event duration plotted in Fig. 2.1c, where the duration is indicated as the mean number of hours of fog per event. A trend toward a summer minimum as well as autumnal and late-winter/early-spring maxima is apparent, although the February-March maximum is based on few events. In general, during the Albany radiation fog season, one can expect fogs of three to four hour duration.

2.3.2 Physical model

An autumnal maximum in the radiation fog frequency is to be expected, primarily due to a sufficient amount of hours available for nocturnal cooling and the availability of adequate moisture from prevailing vegetation. We postulate that a physical model can be formulated to explain the seasonal trend in Albany radiation fog occurrence as a balance between the amount of cooling available (δT_A) and the amount of cooling necessary (δT_N) to saturate the air,

$$f = \delta T_A - \delta T_N , \quad (2.1)$$

where f is the monthly climatological radiation fog frequency for Albany for the years (1970 - 1979):

$$f = \begin{matrix} \text{J} & \text{E} & \text{M} & \text{A} & \text{M} & \text{J} & \text{J} & \text{A} & \text{S} & \text{O} & \text{N} & \text{D} \\ .007 & .021 & .007 & .021 & .056 & .063 & .056 & .119 & .252 & .308 & .091 & .000 \end{matrix} .$$

Utilizing mean monthly climatological weather observations (from LCD's), Eq. (2.1) can be expanded to yield detailed expressions for the δT_A and δT_N . The available cooling can be expressed as a balance between the cooling of the air due to nocturnal radiation and its offset produced by turbulence, applied over the length of the night. We assume here that turbulence is some linear function of wind speed. This available cooling may be thought of as the cooling potential of the surface air. The δT_N term is the amount of cooling necessary to bring the air to saturation given an initial saturation deficit ($q_s - q$). Thus Eq. (2.1) becomes,

$$f = a_0 + \underbrace{\left[(a_1 R_n - a_2 U) t_n \right]}_{(\delta T_A)} - \underbrace{\left[a_3 \frac{(q_s - q)}{\frac{\partial q_s}{\partial T}} \right]}_{(\delta T_N)} , \quad (2.2)$$

where R_n is the net radiation at 0100 LST, U is the wind speed (0100 LST), t_n the length of night, q_s the saturation specific humidity (1600 LST), q the specific humidity (1600 LST), T the temperature (1600 LST), and a_n are constants. R_n was calculated using Brunt's (1932) empirical expression,

$$R_{no} = \sigma T^4 (1 - a - b\sqrt{e}) , \quad (2.3)$$

where σ is the Stefan-Boltzmann constant, e is the vapor pressure (1600 LST), and $a(=0.6)$ and $b(=0.042)$ are constants. Eq. (2.3) is usually corrected for the presence of cloud cover such that,

$$R_n = R_{no} (1 - 0.76 \eta), \quad (2.4)$$

where η is the fraction ($0 \leq \eta \leq 1$) of the sky covered with cloud.

Fig. 2.2 shows the result of fitting a function of the form of Eq. (2.2) to the observed radiation fog frequency. The solid curve shows the result of the multivariate least-squares regression technique used, and is represented by Eq. (2.2) with $a_0=0.089$, $a_1=0.013$, $a_2=0.0052$, and $a_3=0.052$. Also shown are the δT_A (dashed) and δT_N (dash-dotted) components, as well as the actual fog frequency values (+'s). The goodness of fit suggests that this physical model represents the seasonal trend in radiation fog occurrence remarkably well. The Albany radiation fog season begins as the cooling potential exceeds the cooling necessary for air saturation. When this trend is reversed the end of the radiation fog season is observed.

2.4 Synoptic patterns

Five key synoptic surface patterns were linked with radiation fog events at Albany during the 1970-79 period. Type 1 (Fig. 2.3a) is typified by a closed-isobar anticyclone where Albany is usually embedded within the first closed isobar (4 mb intervals). With the type 2 situation (Fig. 2.3b), an open ridge extends into the region (and usually over much of the northeast), often from a well-defined high pressure cell. Occasionally, mesoscale ridging follows a cold (or more often an occluded) front or trough passage, defining fog type 3 (Fig. 2.3c). Type 4 (Fig. 2.3d) occurs when a weak or dissipating frontal zone is in the local vicinity and type 5 (Fig. 2.3e) is associated with a col.

The monthly distribution of the radiation fog events associated with these five synoptic patterns is presented in Table 2.1. Type 1 is the dominant fog-forming situation accounting for just over 40% of all radiation fogs. Following in order are type 2 (21.7%), type 3 (16.1%), type 4 (12.2.3%), and type 5 (9.1%). The closed high (type 1) and major ridge (type 2) situations often lead to more "textbook" radiation fogs, where fog evolves in response to several nocturnal hours of light wind and mostly clear skies. Each of these two types shows an autumnal peak accounting for over 70% of their respective annual occurrences. Type 4 fogs also exhibit a peak in frequency (68.4%) during the autumn months. Ridging behind a frontal zone or trough (type 3) and the col (type 5) tend to be

less seasonally dependent, with the summer and fall months encompassing over two-thirds of these fogs.

Table 2.1. Monthly distribution of heavy radiation fog events by synoptic type (1970-1979)

| Type | J | F | M | A | M | J | J | A | S | O | N | D | Total |
|-------|---|---|---|---|---|---|---|----|----|----|----|---|-------|
| 1 | 0 | 2 | 0 | 0 | 1 | 3 | 1 | 6 | 24 | 16 | 5 | 0 | 58 |
| 2 | 0 | 0 | 0 | 0 | 3 | 0 | 4 | 2 | 5 | 14 | 3 | 0 | 31 |
| 3 | 0 | 1 | 0 | 2 | 4 | 1 | 2 | 5 | 2 | 6 | 0 | 0 | 23 |
| 4 | 0 | 0 | 0 | 0 | 0 | 3 | 0 | 2 | 4 | 6 | 3 | 0 | 18 |
| 5 | 1 | 0 | 1 | 1 | 0 | 2 | 1 | 2 | 1 | 2 | 2 | 0 | 13 |
| Total | 1 | 3 | 1 | 3 | 8 | 9 | 8 | 17 | 36 | 44 | 13 | 0 | 143 |

For the type 1 and 2 fog situations, location of the center (or ridge axis) of the surface anticyclone relative to the station location, appears to be an important factor (Table 2.2). A significant number of these radiation fogs occur when the center of the high pressure cell or major ridge axis is situated over Albany. The position of the high pressure center or ridge east to southeast of the station also seems to be favorable for fog occurrence.

Table 2.2. Surface high pressure center (Type 1) or major ridge axis (Type 2) location relative to Albany, New York

| Type | OC | N | NE | E | SE | S | SW | W | NW |
|-------|----|---|----|----|----|---|----|---|----|
| 1 | 20 | 4 | 6 | 11 | 5 | 5 | 3 | 2 | 2 |
| 2 | 22 | 0 | 0 | 2 | 5 | 1 | 0 | 1 | 0 |
| Total | 42 | 4 | 6 | 13 | 10 | 6 | 3 | 3 | 2 |

Table 2.3 introduces the averaged characteristics of the radiation fog events by synoptic type. Each type 1, 2 and 5 radiation fog averages a little over three hours in duration, and in more than half of these cases visibility declined to what is arbitrarily defined here as the "severe" fog level (visibility less than or equal to one-sixteenth mile). These three surface synoptic patterns account for over eighty percent of severe radiation fogs at Albany. The fog severity ratio (FSR), defined as the ratio of the number of hours of severe fog to the number of hours of heavy fog, indicates that type 3 and 4 fogs are the least likely to produce periods of severe fog. Type 3 and 4 fogs also persist about one hour less, with only 17% and 33% of these events being severe, respectively.

Additional SWO's, such as the vector-averaged wind speed, initial pressure, and initial temperature, tend to reflect the nature of the synoptic situation. The surface pressure is higher when situated near the anticyclone center or ridge, while the lowest values are observed following front or trough passages. Lower initial temperature is linked to those situations most favorable for sustained periods of radiational cooling. As much as a five degree difference (warmer) is exhibited by the frontal types, most likely owing to restricted cooling by cloud cover or upper level moist layers for part of the evening. Wind speed is minimum for the dominant synoptic patterns (types 1 and 2).

The prevailing vector-averaged wind directions during fog are calm (39.9%), southerly (20.3%), northerly (15.4%), and north-easterly (13.3%). These principal directions are a direct consequence of the high pressure location reported in Table 2.2. Albany is situated at the junction of the Mohawk (oriented east-west) and Hudson (north-south) River valleys. In the absence of significant surface pressure gradients, the Hudson valley generally dictates the wind direction.

An investigation into the role of measurable (greater than or equal to 0.25 mm) precipitation prior to fog development indicated only a modest influence. Table 2.4 shows the percentage of fog events for which measurable precipitation was observed 12, 24, 48, and 72 hours prior to the onset of fog. Overall, less than one-third of fog events occur within 24 hours after measurable precipitation, and approximately one-half within 48 hours. For all types the percentage increases with time. This is more likely a result of the natural precession of synoptic systems. Note that type 3 fogs exhibit a greater tendency to form after precipitation events owing to the frontal or trough passage itself. Here the additional ground moisture provided helps promote fog formation, with shorter periods of radiational cooling usually observed in these post-frontal patterns. Fog intensity showed little correlation with preceding precipitation measurements.

Table 2.3. Averaged characteristics of heavy radiation fog events
by synoptic type, 1979-1970, Albany, New York

| | Synoptic (Fog) Type | | | | | |
|---------------------|---------------------|-----------------|-----------------|-----------------|-----------------|-----------------|
| | <u>1</u> | <u>2</u> | <u>3</u> | <u>4</u> | <u>5</u> | <u>ALL</u> |
| t_h [hh.mm] | 3.09 (3.10) | 3.24 (2.12) | 1.58 (1.55) | 2.46 (2.10) | 3.07 (2.52) | 2.58 (2.40) |
| N_s/N_h | 0.50 | 0.55 | 0.17 | 0.33 | 0.62 | 0.45 |
| FSR | 0.28 (0.35) | 0.31 (0.34) | 0.09 (0.23) | 0.15 (0.30) | 0.37 (0.37) | 0.25 (0.34) |
| V_{min} [km] | 0.16 (0.15) | 0.14 (0.14) | 0.26 (0.15) | 0.21 (0.15) | 0.15 (0.13) | 0.18 (0.15) |
| U [$m\ s^{-1}$] | 0.73 (0.90) | 0.91 (0.95) | 1.32 (1.32) | 1.60 (1.40) | 1.54 (1.03) | 1.05 (1.11) |
| P_o [mb] | 1025.6 (4.4) | 1022.2 (5.6) | 1014.4 (5.0) | 1019.7 (4.6) | 1017.4 (5.0) | 1021.6 (6.3) |
| T_o [C] | 7.4 (4.3) | 7.5 (5.4) | 12.1 (4.8) | 11.8 (5.0) | 10.0 (6.4) | 9.1 (5.3) |

where:

| | |
|---------------------|---|
| t_h [hh.mm] | is the duration of heavy fog (in hours.minutes) |
| N_s/N_h | is the ratio of number of severe fog events to heavy fog events |
| FSR | is the Fog Severity Ratio (see text) |
| V_{min} [km] | is the minimum visibility measured during fog event |
| U [$m\ s^{-1}$] | is the average wind speed during fog event |
| P_o [mb] | is the surface atmospheric pressure at fog onset |
| T_o [C] | is the surface air temperature at fog onset. |

Table 2.4 Percentage of heavy radiation fog events following measurable precipitation, 1970-1979, Albany, New York

| <u>Type</u> | <u>Precipitation within:</u> | | | |
|-------------|------------------------------|-----------------|-----------------|-----------------|
| | <u>12 hours</u> | <u>24 hours</u> | <u>48 hours</u> | <u>72 hours</u> |
| 1 | 0.0 | 13.8 | 41.4 | 60.3 |
| 2 | 0.0 | 22.6 | 45.2 | 51.6 |
| 3 | 47.8 | 82.6 | 87.0 | 91.3 |
| 4 | 16.7 | 27.8 | 38.9 | 61.1 |
| 5 | 23.1 | 23.1 | 53.8 | 69.2 |
| All Types | 11.9 | 29.4 | 50.3 | 64.3 |

2.5 Diurnal characteristics

A diurnal cycle of fog formation on land was probably first investigated by Taylor (1917). He hypothesized that radiation-type fogs formed sometime during the night in the location where they were observed in the morning. Additionally, Taylor proposed a radiation fog forecasting scheme based on late-afternoon and early-evening synoptic observations.

To reveal the diurnal nature of radiation fogs at Albany, the frequency of hourly radiation fog observations for our 143 fog events is plotted versus local standard time (LST) in Fig. 2.4. The graph shows a nearly monotonic increase in fog observations until a peak is reached between 0500 and 0600 LST. After 0700 LST, a rapid decline in fog occurrence is noted. From noon to midnight there is an insignificant contribution to the fog observations.

Recent radiation fog studies by Pilié et al. (1975), Roach et al. (1976), Mason (1982), and Meyer et al. (1986) indicate that increasing solar radiation associated with sunrise can act to initially promote, enhance and eventually dissipate radiation fog. This scenario manifests itself well in the climatological data. Fig. 2.5 shows the observations of radiation fog (solid line) as given in Fig. 2.4, but now plotted relative to sunrise time. Also shown are the time of fog development (dashed line) and fog dissipation (dotted line) relative to sunrise time. Notice the peak in fog observations within the first hour after sunrise. Fog formation and fog dissipation also exhibit peaks within the hour before sunrise and within the second hour after sunrise respectively. Fog formation generally will occur within six hours before sunrise and fog dissipation is complete within four to six hours after sunrise.

2.6 Implications for fog forecasting

The results of this study should aid the forecaster in determining if predicted conditions (i.e., surface synoptic patterns and surface weather parameters) might be favorable for radiation fog formation. Since this information is climatological in nature, there are practical limits in its operational applicability. For example, we have not yet attempted to discern when these surface synoptic patterns occur without fog developing. Perhaps by utilizing the physical model presented, real probabilities could be assigned for observing a radiation fog given a particular synoptic situation. This will be the focus of future work.

The information gained in this work can be used with confidence to practically eliminate a forecast of fog for an obvious non-fog pattern. In general, we believe the weather analysis methodology developed, and some of the trends themselves, would apply to other inland regions of the northeastern United States.

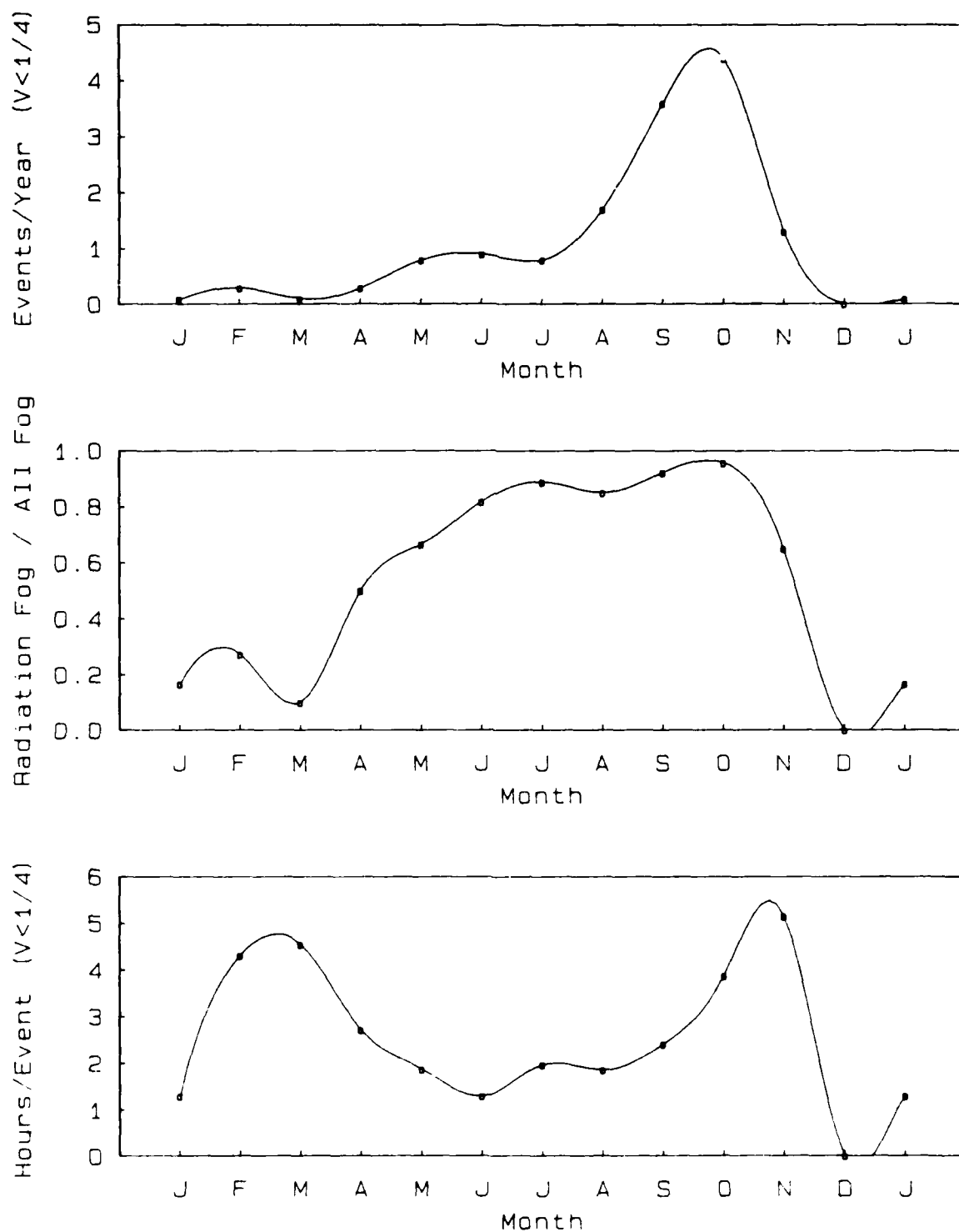


Figure 2.1. Monthly frequency of radiation fog characteristics at Albany, New York, averaged over the period 1970-1979. TOP: Number of fog events per year; MIDDLE: Fraction of all fogs which are radiation fogs; BOTTOM: Number of hours of fog per each fog event.

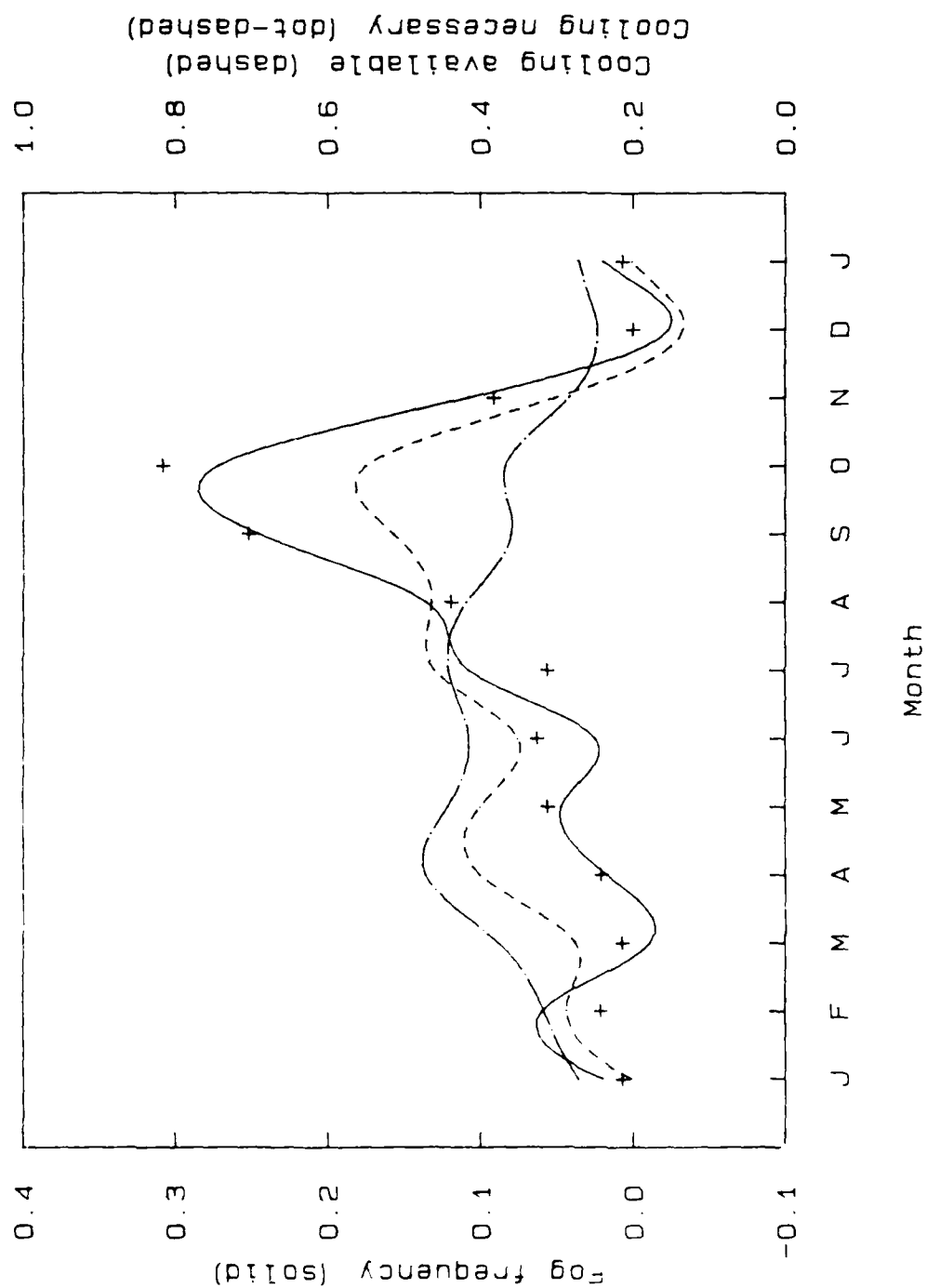


Figure 2.2. Physical model describing the observed radiation fog monthly frequency (+'s) at Albany, New York averaged over the period of 1970-1979. SOLID: Model fit to the fog frequency using Eq. (2.2). Multivariate least-squares regression yields $a_0 = 0.089$, $a_1 = 0.013$, $a_2 = 0.052$. DASHED: Cooling available. DASH-DOTTED: Cooling necessary.

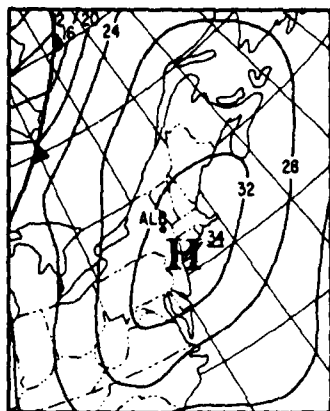


Figure 2.3a. Example of type 1--
closed high. (12Z 26 SEP 1973).

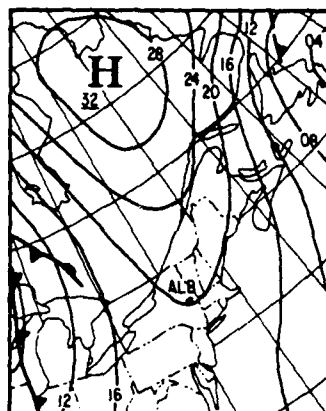


Figure 2.3b. Example of type 2--
major ridge. (12Z 3 OCT 1978)

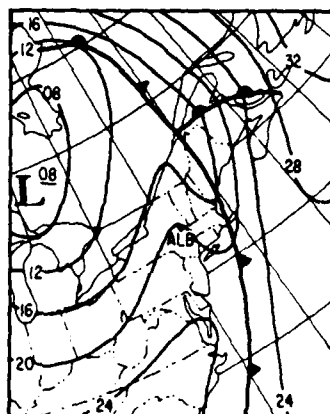


Figure 2.3c. Example of type 3--
post-frontal ridging. (12Z 3 APR 1971)

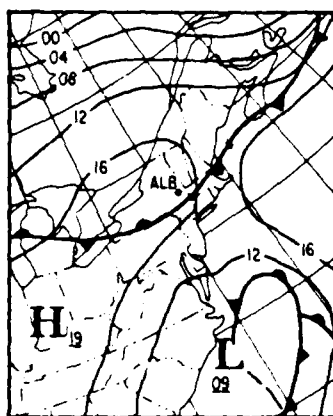


Figure 2.3d. Example of type 4--
weak front. (12Z 27 OCT 1977)

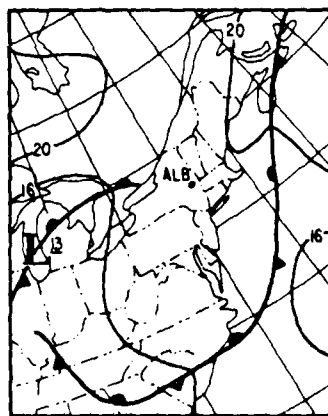


Figure 2.3e. Example of type 5--
col. (06Z 31 JUL 1973)

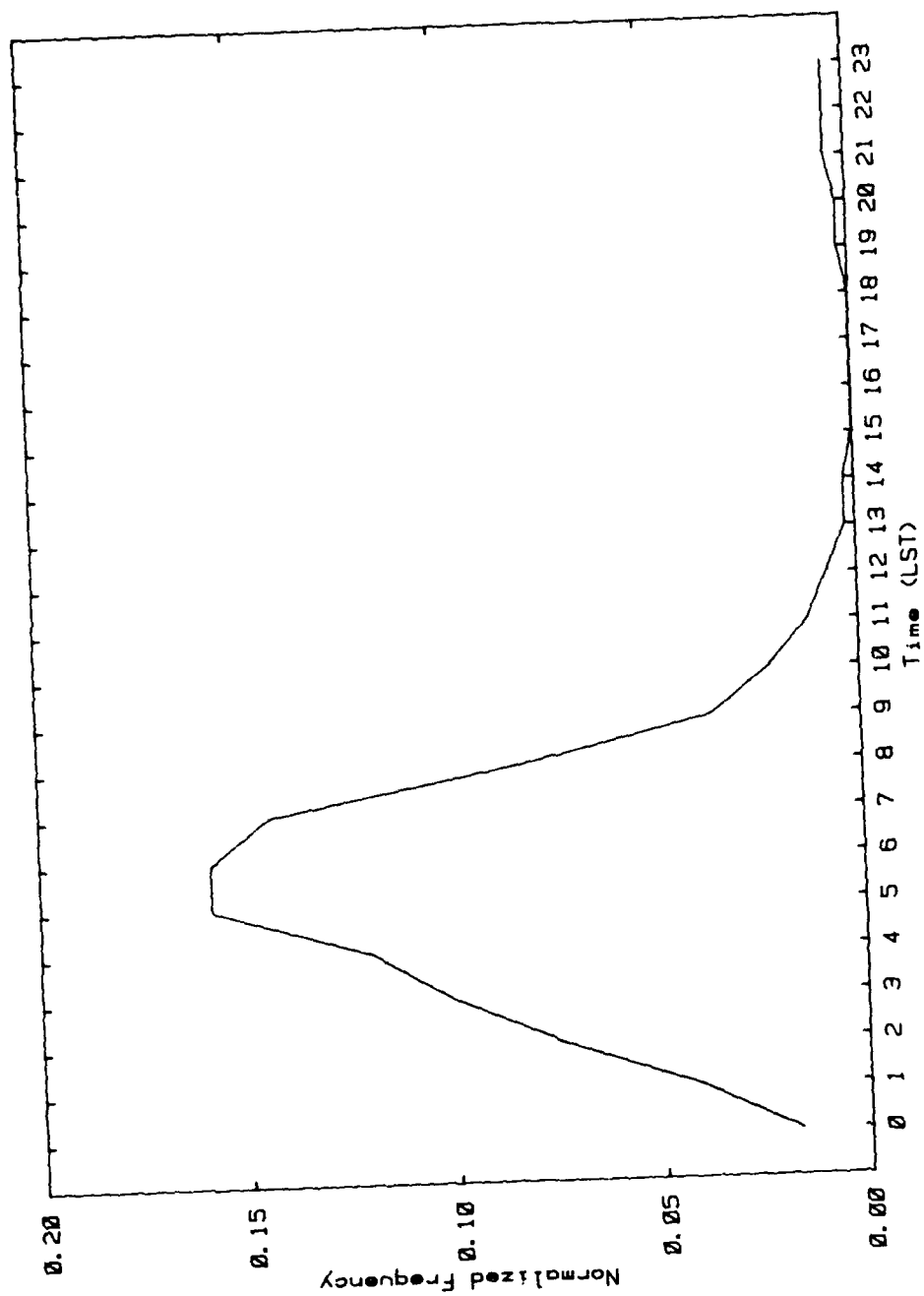


Figure 2.4. Normalized frequency of hourly radiation fog observations at Albany, New York averaged over the period 1970-1979.

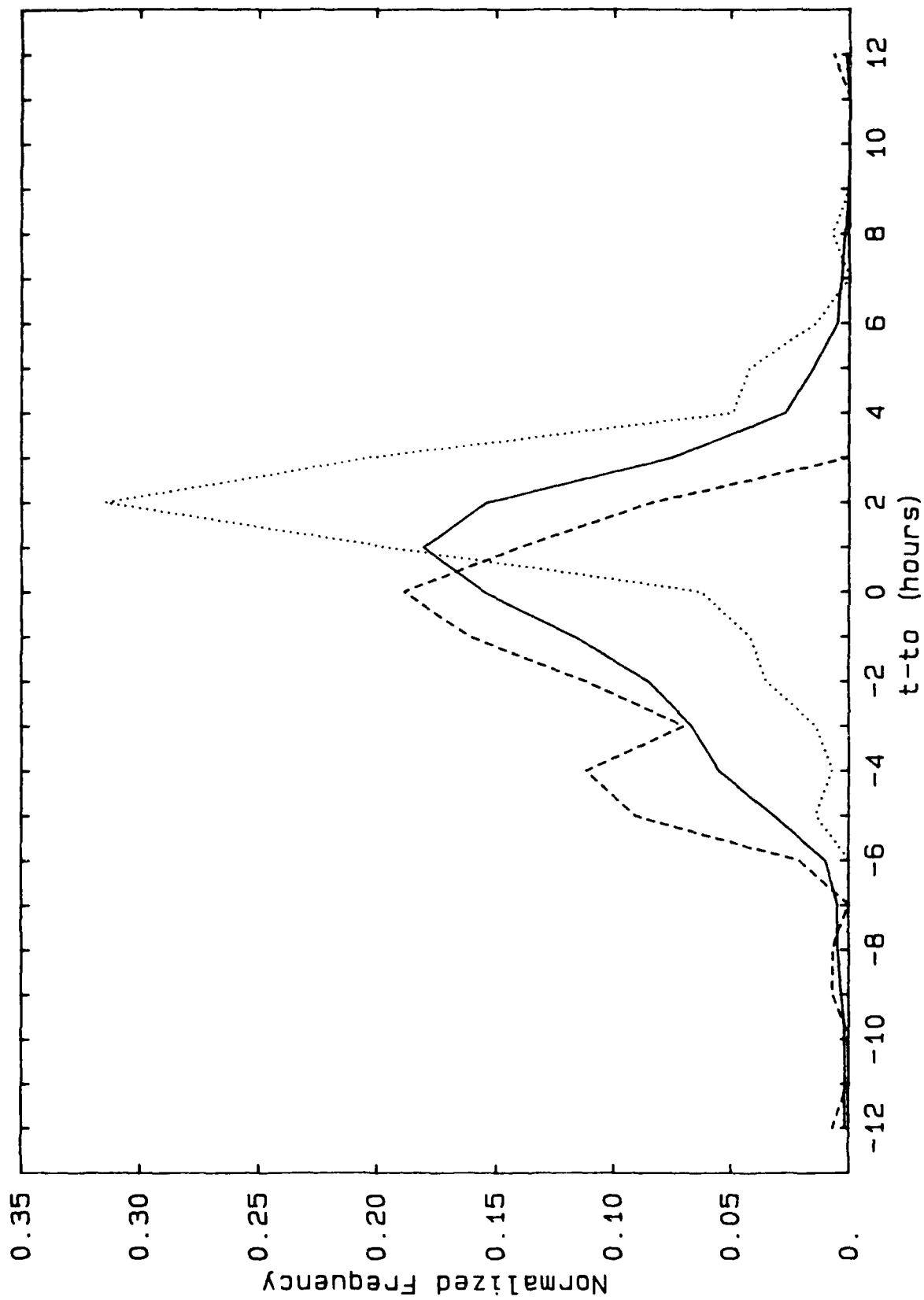


Figure 2.5. Observations of radiation fog (solid line) as given in Fig. 2.4, but now plotted relative to sunrise time. Also shown are the time of fog development (dashed line) and fog dissipation (dotted line) relative to sunrise time.

3.0 Hudson Valley Fog Environments

3.1 Introduction

We seek to identify ambient conditions that control fog development and maintenance, referred to here as fog environments. Important elements of these environments include vertical boundary layer temperature, humidity, and wind structure, radiative cooling rate profiles, and horizontal heat and moisture transport, as well as surface fluxes. Our thesis is that fogs only occur in supportive, predictable environments, and that to understand fog onset time and ultimate thickness we must consider mesoscale heat and moisture budgets in the Hudson river valley as well as surface conditions. Since advective terms are sometimes an important component of these budgets, local wind circulations can also be important.

Albany, New York (42.75°N, 73.8° W), the site of the experiments presented here, lies near the confluence of the Hudson and Mohawk rivers. To the north, the axis of the Hudson merges with the Champlain valley to provide an approximately north-south channel extending nearly 500 km from the Atlantic to the Canadian border. For part of this distance the Hudson-Champlain valley is paralleled by the Connecticut River valley. Both valleys are susceptible to occurrences of widespread radiation fogs. At Albany, the Hudson valley is approximately 30 km wide, with high ground on either side of the valley eventually rising 200-300 m above the river. It should not be surprising that local and regional wind systems along the river valleys can be important, particularly in the absence of strong synoptic effects which are characteristic of nights with radiation fog.

Radiation fogs at Albany occur most frequently within an hour or two of dawn on fair autumn nights (Meyer and Jiusto, 1982). However, even given what appear to be ideal conditions, when there are light surface winds on clear nights with a large synoptic high pressure center nearby, some nights yield persistent fogs and others stay mostly clear, showing only patchy fogs at best. Recent observational and modeling studies of fog have focussed on the role of surface layer turbulence properties in influencing fog development given adequate radiative cooling (Forkel et al., 1987). These studies have led to detailed parameterizations of fog microphysics, radiative exchange, and, to a lesser extent turbulent mixing, but initial conditions that associate with radiation fog development have received much less attention.

Six general, practical, topics are central to any discussion of radiation fogs: 1) Fog onset time; 2) Final fog thickness; 3) Areal extent of fog; 4) Internal fog dynamics; 5) Visibility reduction and cloud microphysics in fogs; and 6) Fog dissipation time. Here we

address primarily the first three considerations, deferring discussion of fog microphysical observations and study of motions inside developed fogs to companion papers. Based on our field experience, we have formulated idealized models descriptive of the mechanisms which we think are important in fog development.

3.2 Conceptual models

Three conceptual models presented below are based on our analysis of case study periods. The models, idealizations based on common features seen in many, but not all cases, summarized the observations.

3.2.1 Approach to saturation

To understand when fog will form we must describe the approach to saturation in the surface and boundary layers. G. I. Taylor (1917) viewed fog formation in the surface layer as a competition between dew deposition and radiative cooling. His plot of dew point depression in the early evening against temperature at Kew, England was an early attempt to describe the fog environment. Taylor and, later, others (i.e., Rodhe, 1962) also noted that turbulent mixing could also prevent, delay, or enhance fog formation. More recently, models including turbulent exchange and radiative cooling (i.e., Oliver et al., 1978; Welch et al., 1986; Musson-Genon, 1987; Turton and Brown, 1987) have included increasingly complicated treatments of turbulent vertical exchange processes, cloud microphysics and radiative cooling.

In this section we estimate the time it takes for a layer to approach saturation. Comparing this time to the length of night is one measure of fog probability. To keep track of various factors contributing to fog development we consider the budget of saturation specific humidity deficit, $(q_s - q)$ (q_s is the saturation and q the observed specific humidity). This balance shows explicitly the contributions of the heat and moisture budgets, since $\partial q_s / \partial t \approx (1/p)[de_s(T)/dT] \partial T / \partial t$ (e_s is the saturation vapor pressure; we assume pressure to be approximately constant). The factor in brackets is clearly the Clausius-Clapeyron equation, $de_s(T)/dT = [\epsilon L_v / RT^2] e_s(T)$, where $\epsilon \approx 0.622$, L_v is the latent heat of vaporization of water, R the gas constant, and T the absolute temperature. The saturation and observed specific humidity budgets can be written:

Saturation specific humidity budget:

$$\partial q_s / \partial t \approx (1/p) [de_s(T)/dT] \{ \partial T / \partial t \},$$

where:

$$\begin{array}{cccccc} \partial T / \partial t = & - \partial R_n / \partial z & - \partial (wT) / \partial z & - v_h \nabla_h T & - W (\partial T / \partial z - \gamma) & + L(c - e) \end{array} \quad (3.1a)$$

1 2 3 4 5 6

Specific humidity budget:

$$\begin{array}{cccccc} \partial q / \partial t = & & - \partial (wq) / \partial z & - v_h \nabla_h q & - W (\partial q / \partial z - \gamma_q) & - (c - e) \end{array} \quad (3.1b)$$

1 2 3 4 5 6

where notation is standard, except that R_n is the net radiation (in kinematic units), γ is the adiabatic lapse rate, γ_q the lapse rate in q , v_h the horizontal wind vector, W the large-scale mean subsidence, and the term $L(c - e)$ represents the thermal effect of condensation (c) minus evaporation (e). We have written the explicit heat budget inside the Clausius-Clapeyron multiplier to emphasize that the importance of cooling in determining the approach to saturation depends on the temperature. Terms in these budgets are: 1) local change; 2) radiative cooling; 3) turbulent flux divergence; 4) horizontal advection; 5) drying or warming effects of large-scale subsidence; and 6) the net effect of condensation or evaporation. The terms 6) are important to the pre-fog environment only if a significant number of aerosols are activated. They can be important to the understanding of the heat balance at the surface, where dew forms (see section 3.2.3 below). G. I. Taylor's "race" between dew deposition and cooling balances term 2 in the q_s equation (Eq. 3.1a) and term 3 in Eq. (3.1b); the turbulent balances included by Rodhe, Oliver et al. and others additionally considered the 3rd term in Eq. (3.1a). Estimates of other terms that are also relevant to radiation fog development at Albany have been made.

3.2.2 Boundary layer model

We can make a very simple, preliminary estimate of fog onset time in the boundary layer by assuming q to be constant with time. This assumption neglects to the first approximation dew deposition, only likely to be appreciable in the surface layer; it agrees well with observations above 20 meters made during the field experiment. In the absence of significant horizontal advection and with a constant total cooling rate, $\partial T / \partial t$, the time it takes for fog formation is given by integrating the relation

$$\partial(q_s - q)/\partial t \approx \partial q_s/\partial t \approx (1/p)[\epsilon L_v/RT^2] \partial T/\partial t, \quad (3.2)$$

from the initial saturation specific humidity, q_{s0} , to the final value at saturation, q , the current value of the specific humidity. We note that the function $1/T^2$ varies only approximately 10% over the range of temperatures encountered when fog occurs and hold it constant during the time integration of Eq. (3.2). This results in a relation between the time it takes to reach saturation, τ_f , the relative humidity at the start, RH_0 , and the total cooling rate, $\partial T/\partial t$:

$$\tau_f \approx [\epsilon L_v/RT^2] \ln(RH_0) [\partial T/\partial t]^{-1}, \quad (3.3)$$

The local net cooling rate, Eq. (3.1a), was assumed to be approximately constant during the time integration.

As a conceptual model, we consider the representative boundary layer state at dusk, a time at which the surface heat flux is zero, going from positive to negative. A convective boundary layer (CBL) grown during the day typically leads to formation of a layer well-mixed in q and in potential temperature. The adiabatic lapse rate in T is reflected in the lapse of q_s . If we impose a typical total cooling rate profile as given in the figure, we arrive at a profile estimate of τ_f , small near the surface where both turbulent cooling and radiative flux divergence are largest, reaching a maximum at the top of the surface layer and a second relative minimum at the maximum afternoon height of the convective boundary layer. A low-level total cooling maximum implies that surface layer fogs should occur first if dew deposition is not significant. For deeper fogs to form above the surface layer, the boundary layer must be moist enough initially and not suffer appreciable dry advection overnight. Since τ_f is also small at the maximum height of the afternoon convective boundary layer, possible appearance of a transient stratus deck there provides another mechanism to prevent fog from forming, as long-wave cooling near the ground would thereby be reduced. Since surface moisture fluxes over land usually become small at night, the initial RH_0 that determines τ_f in the boundary layer is the result of afternoon convective mixing. Thus, the likelihood of saturation throughout the stable boundary layer may depend strongly on events (for example, CBL growth and moistening) that occur on the afternoon preceding fog rather than on existing conditions at sunset or evolution of surface boundary conditions during the night. This indicates that soil moisture, for example, should correlate with fog likelihood because of moisture delivered to the atmosphere during the afternoon. Its role during the night on which the fog occurs is small.

3.2.3 Surface layer model

The surface layer plays an important role in the initial stages of fog formation. The tension between the effects of surface layer cooling and moisture deposition is frequently cited as the central question in surface fog studies. Oliver et al. (1978) present a modern similarity interpretation of Taylor's (1917) criterion for existence of turbulence-dominated surface fogs. They concluded that turbulent heat fluxes can dominate radiative cooling in layers deeper than a few meters only in the presence of appreciable winds.

We agree that the heat and moisture balances are important to understanding the approach to saturation in the surface layer, but we do not see that dew deposition is crucial to determining fog onset time for the Albany cases. We see the following characteristic sequence of surface layer events on likely fog nights: With waning short wave radiation in the late afternoon, net radiation (positive upwards, like all quantities in this paper) becomes strongly positive. Soil heat flux cannot respond rapidly enough to balance the net radiation, and the surface heat budget is maintained by a negative surge in turbulent heat flux, which continues until eddy motions are finally damped out by steadily increasing surface layer stability. During this initial period of turbulence-dominated transport, moisture flux is still positive. As the evolving stable surface layer decouples from the boundary layer above, and moisture flux convergence into the surface layer leads to a jump in specific humidity. Each process diminishes the saturation deficit, reducing τ_f . After the initial period of rapid cooling and moistening, turbulent processes become intermittent, and the surface layer cools at a rate determined primarily by the radiative flux divergence. Dew deposition during this period is not sufficient to increase τ_f appreciably. Occasional lulls lead to brief periods of rapid cooling and reduced visibility. When the surface layer is shallow enough, gusts can warm the layer and increase visibility. After saturation is reached, moisture deposition keeps pace with falling saturation specific humidity.

We can distinguish between the period of turbulence-dominated cooling and moistening and the later period of radiatively-dominated cooling by reference to the temporal curvature of the surface-layer temperature. Supposing transport terms to be small and with conditions of horizontal homogeneity, integrating Eq. (3.1a) from the surface to z_s , a measure of the surface layer thickness, and taking the time derivative yields

$$z_s \partial^2 T / \partial t^2 = \partial / \partial t (w \theta_o - w \theta_s) + \partial / \partial t (R_{no} - R_{ns}) ,$$

where subscripts o and s refer to $z = 0$, and $z = z_s$, respectively. During the early-evening surface layer transition, we ignore $w \theta_s$ in comparison to the surface term. We approximate the heat flux budget, $\partial w \theta_o / \partial t \approx -\sigma_w^2 \partial T / \partial z + (g / \Theta_o) \sigma_\theta^2$, and arrive at:

$$z_s \partial^2 T / \partial t^2 = - \sigma_w^2 \partial T / \partial z + (g / \Theta_0) \sigma_\theta^2 + \partial / \partial t (R_{no} - R_{ns}) \quad (3.4)$$

This relation shows that temporal curvature is negative when the first term dominates and positive when the third, radiative term dominates. During the transition period, $\partial T / \partial z$ grows rapidly enough to compensate for diminishing σ_w^2 ; the σ_θ^2 term is probably important only at the end of the transition period. Afterwards, σ_w^2 , σ_θ^2 , and $\partial R_{no} / \partial t$ become small, and we expect an approximately linear cooling rate. Then the τ_f estimate made in the previous section applies. The changes in curvature of the temperature trace and the jump in specific humidity, illustrated in the sketch of our conceptual model, conform to those seen in many observations. They provide a simple way to identify the early-evening transition in routinely available data.

After fog forms, conditions in the surface layer may reflect motions occurring in the deeper saturated layer. This reversal of roles happens as the layer changes from stable to approximately neutral stratification. Since turbulent fluxes are small above the surface inversion, heat and moisture flux divergence in the layer is due primarily to surface fluxes.

3.2.4 Local wind model

Inland radiation fogs occur most frequently in valleys; to ignore channelling effects and local winds is to neglect an important part of the problem. Winds in river valleys are frequently observed to be channeled along the valley axis. Gross and Wipperman (1987) have demonstrated this effect convincingly in the wide, upper Rhine valley in Germany, and there is every reason to believe that similar flows occur in New York. When there is a significant along-valley pressure gradient (cross-valley geostrophic wind component strong), the effect of valley side walls is to produce a small cross-valley pressure gradient that opposes the Coriolis force. This hypothetical mechanism contrasts with the daytime turning toward lower pressure that friction alone can accomplish, though this, too, can be enhanced by channelling due to roughness differences in and around the valley. We consider three important dynamic layers in the Hudson valley nocturnal boundary layer: 1) A stable surface layer, in which turbulent activity is presumed intermittent, reaching approximately to 20 m and underlying 2) a boundary layer in which channelling can occur when along-valley pressure gradients are sufficient. The second layer reaches approximately to 150 m, blending into 3) a region of rapid geostrophic adjustment. Observations indicate that after only a few hours, less time than the 18 hour inertial period at Albany, winds at 250 m altitude correspond well to those at 850 mb. By exerting control

on humidity, this layer can determine the maximum fog height. Rotation toward the westerly geostrophic flow at 850 mb usually advects in dry air during the autumn. Dynamical maintenance of channelled, moist southerly flow in the boundary layer can prevent dry advection from deterring fog onset. Thus, it is conceivable that fairly strong boundary-layer winds in the valley could actually promote, rather than inhibit, fog formation.

3.3. Some conclusions

Fogs in the Hudson valley occur when the environment supports them, but determination of the supportive environment involves more than the traditionally considered surface layer observations. Deep fogs at Albany and along the valley are boundary layer phenomena, and they occur when boundary layer circulations are either weak or are such that sufficient moisture is maintained above the surface layer. To the first approximation, the surface layer is effectively decoupled from the boundary layer on many fog nights, and the presence of decreased visibility below 20 m offers little information about the likelihood of deepening fogs later. We suggest that modelers of fog phenomena test the simplest version of their model to verify or refute our hypothesis that initial moisture conditions determine fog onset time and probable thickness before extremely complex schemes to predict droplet microphysics and radiative heat transfer schemes are employed.

4.0 Observations of Droplet Spectra in Radiation Fog

4.1 Introduction

Measurements of fog drop spectra have been conducted for the purpose of determining the influence of the drop size distribution on optical and infrared transmission as well as on liquid water transport. Most early measurements were conducted using impaction type devices which have an intrinsic drop size limitation and sampling was conducted on an intermittent basis. With the development of optical particle counters and modern computers, it has become possible to acquire drop size data over a wide size range on a continuous basis. The instrument used in this study was the FSSP-100 developed by Particle Measuring Systems, Knollenberg (1981). While there are limitations to this instrument (Pinnick et.al., 1981; Cerni, 1981; Dye and Baumgardner, 1984; Baumgardner, 1983), it does provide an opportunity to study the evolution of drop spectra by virtue of its ability to provide nearly continuous samples of drop spectra. Comparison of this instrument to other methods suggests that with care in calibration and operation, the instrument can provide consistent measurements with errors comparable to other drop measurement devices. During the studies reported here, a ground based, aspirated FSSP-100 was used for measurements near ground level (1.5 m). The instrument was operated with alternating 20 second samples on the smallest size range (0.5 - 8.0 μm) and the largest size range (3.0 - 47.0 μm) accumulated over a two minute sample interval. This approach was taken to provide as much detail as possible over the small size range while sampling a volume large enough to insure that counting errors at the large sizes were a minimum.

One of the problems associated with the use of drop size spectrometers is the large amount of data accumulated during an experiment and the need to display the results in a manner that clearly shows changes in drop spectra both with size and time. Several types of displays such as various derived quantities at a given size as a function of time or as contours of the derived quantity as a function of size and time. Both of these displays have limitations which have been overcome by displaying drop spectra and spectra of derived quantities as three dimensional plots with axes representing concentration, diameter, and time. Fig. 4.1 is an example from two fog events. The logarithm of the number density is plotted against time and diameter. While this display does not preserve concentration in the size-concentration plane, it does allow the display of details of the spectrum at large sizes where concentrations decrease rapidly with size.

4.2 Evolution of drop spectra during dense fog

Fig. 4.1a is typical of a shallow fog (height ~ 50 m) while Fig. 4.1b is an example of a deep fog (height ~ 130 m). Each of these plots is a display of drop spectra measured during periods of dense fog lasting for 5 hours or more. At the small end of the spectra, the concentrations are similar between cases. Also notable is the structure in the size distribution at the smallest sizes, which is preserved throughout the measurement period. This structure is attributable to the non-monotonic nature of the scattering characteristic of the instrument. While the shape of the distribution at these small sizes may not be very accurate, the measurements do show the presence of a large concentration of unactivated haze droplets common at the low supersaturations encountered in fogs. By contrast, the spectra at large sizes are quite different. For the case of 25,26-Sep-1982 (Fig 4.1a), few drops larger than 40 μm diameter are observed whereas the case of 30-Sep-1982 (Fig 4.1b) there are drops recorded out to the upper limit of the instrument (47 μm). During the time period between 0500 to 0830 (local time) the shape of the spectra indicates that a considerable number of drops with sizes beyond the measurement limit were present in the fog.

Also of interest is the transition that occurs around 0500 for the case of 30-Sep-1982. This transition from a spectrum of the type more common to the shallow fog of Fig 4.1a to a broader spectrum occurs during a period when the fog thickens from a shallow surface fog to a deep fog. Also of interest is the transition which occurs around 0700. During this later stage of the fog, the spectrum broadens while the mean size decreases. This transformation is attributable to the effects of surface heating by the sun as well as an increase in turbulence as shown by the increase in vertical velocity fluctuations. These two cases are typical examples of the types of spectra observed during the field program. Details of the evolution of spectra vary considerably from case to case but general features seem to be correlated with fog depth.

4.3 Models of Fog Drop Spectra

Fog drop number distributions have been described using among others the lognormal and gamma distribution functions (Tampieri and Tomasi, 1976; Low, 1979). The process of fitting these functions is often complicated by the presence of a haze distribution or by truncation of the spectra at large sizes by the instrument. Rather than taking the conventional approach of fitting the number distribution, it is more appropriate to work with the mass or liquid water content distribution. The advantage of this procedure is that the influence of the small drops is minimized while the model parameters are

determined by the part of the drop spectrum most responsible for fog water content as well as optical extinction.

Examination of many individual mass distributions from dense fog periods suggested that the distributions would be well described by the lognormal distribution function. To test the applicability of this approach to a long fog period, three dimensional plots of the normalized mass distribution were plotted for these cases (Fig. 4.2). The symmetric character of the distributions supports the choice of the lognormal function. Moreover, because of the normalization, the relative constant shape of the curves suggests that the distribution parameters tend to remain constant over extended periods of time. Certain features identified earlier such as the transition at 0630 for the 30-Sep-1982 case become much more apparent when the data is displayed in this fashion. Based on these results, the data was further analyzed to determine the values of the lognormal distribution parameters for each individual spectrum.

The procedure followed here differs from that used by Lala et.al. (1986) in that the function fit to the cumulative distribution of mass is performed as a linear problem in a log-probability coordinate system rather than as a problem of fitting a quadratic to the logarithm of the density function. By limiting the data used for determining the distribution parameters to a range from $-\sigma_g$ (geometric standard deviation) to $+2\sigma_g$ about the mass median diameter (D_{g3}), the best fit to the data in the region of interest was insured. To allow for the truncation of the data by the instrument, corrections were applied to the data and a new solution for the distribution parameters was found. This iterative process was continued until the calculated parameters converged to a constant value. This procedure works well for most distributions with the exception of times when rapid transitions were occurring when the distribution was either multimodal or dominated by the haze distribution.

Results of the analysis of the two cases presented above is presented in Fig. 4.3. The lower panel is a plot of the mass median diameter along with the diameters corresponding to the 5% and 95% limits of the model distribution function. The second panel is a plot of the σ_g . The third panel is a plot of the number of drops accounted for by the curve fit to the large drop mode along with the total number of drops larger than $2\text{ }\mu\text{m}$. The fourth panel is a plot of the liquid water content computed from the spectrum along with the water content accounted for by the model distribution. For the case of 25-Sep-1982 (Fig.4.3a), the near constant shape of the distribution is shown by the nearly constant value of the mass median diameter as well as the uniform width of the band defined by the 5% and 95% diameters. By contrast, the case of 30-Sep-1982 (Fig. 4.3b) clearly shows the transition from a narrow distribution before 0530 to a much broader distribution.

During the later part of the event after 0730, the width of the distribution remains about the same but the mass median diameter has decreased. Corresponding to this is an increase in the GSD. In both cases, the number of droplets accounted for by the model is much less than the total droplet concentration but the liquid water content is closely predicted by the function fit. This is an indication of the minor contribution of small haze drops to the liquid water content of fogs.

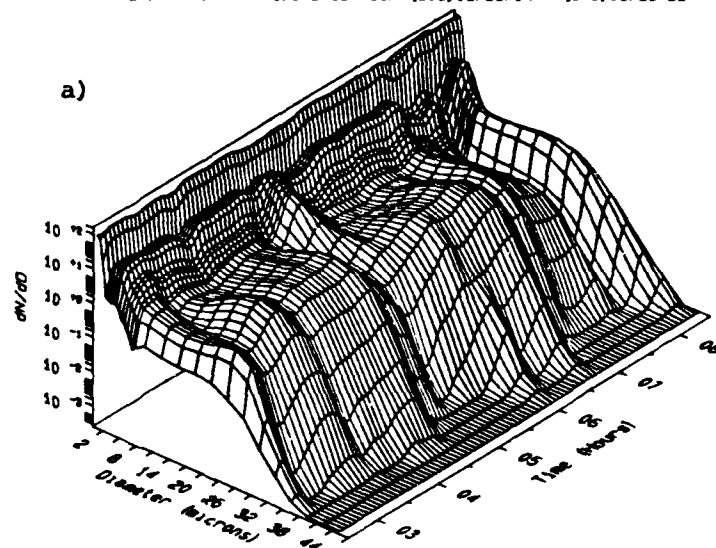
Over the whole period chosen for analysis, the relative uniform behavior of the median diameter and the σ_g in the presence of large fluctuations in the liquid water content suggests that the changes in water content are primarily due to changes in the number of drops in the mass mode. To verify this, local time rates of change of water content were compared with changes in the model predicted water contents due to changes in the number of drops. For the two cases shown here, changes in the water content due to variation in the number of drops in the model distribution accounted for 80% and 75% of the variation for the 25-Sep-1982 and 30-Sep-1982 cases respectively. The majority of the residual variability was accounted for by changes in the mass median diameter.

Thus, over relatively long periods of time, the processes of nucleation, growth by diffusion, and vertical transport by organized circulations and turbulence, act to produce distributions of water content which have nearly steady values of mass median diameter and σ_g , but highly variable droplet concentrations. The balance of the processes involved which leads to this characteristic is not evident from these data. Model calculations by Baroniti and Elzweig (1973) suggest that the nature of the observed distribution at the surface is predominantly controlled by the supersaturation at the fog top, as well as the rate of creation of new drops controlled by the availability of nuclei.

Other investigators have tried to parameterize optical extinction, sedimentation flux, and infrared transmission in fogs in terms of liquid water content (Eldridge, 1971; Corradini and Tonna, 1979; Kunkel, 1984; and others). Data used in these studies came from a variety of data sets and from different fog events, generally leading to power functions as the best fit. Kunkel (1984) used drop spectrometer data from advection fogs and found that linear relations for the sedimentation flux worked better than the power functions for his data set. As a consequence of the uniformity in shape observed here, one would expect that a linear relationship for extinction and liquid water flux would provide the best description. Tests of this hypothesis for the sets of data used here confirm this. Thus, one can conclude that simpler linear parameterizations are valid, but the constants used may depend on the fog type and thickness because of its role in controlling the shape of the drop size distribution function. Use of generalized parameterizations in fog models in an attempt to account for all possible fog types may lead to erroneous results. Future

work should concentrate on understanding the mechanisms responsible for the formation of uniform distribution shapes and this information should be employed in models as simple formulations which depend on fog thickness as well as other variables.

25, 26-SEP-82 Time Interval: [269]02:32:04 - [269]08:29:52



30-SEP, 1-OCT-82 Probe a Time Interval [274]04:46:21 - [274]09:56:44

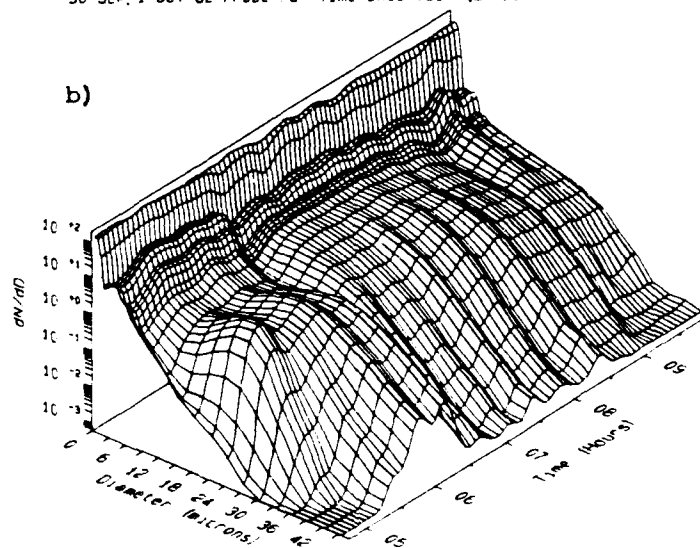


Figure 4.1 (a,b). Fog drop number distributions versus time during periods of dense fog on a) 25,26 Sept. 1982, b) 30 Sept.-1 Oct. 1982.

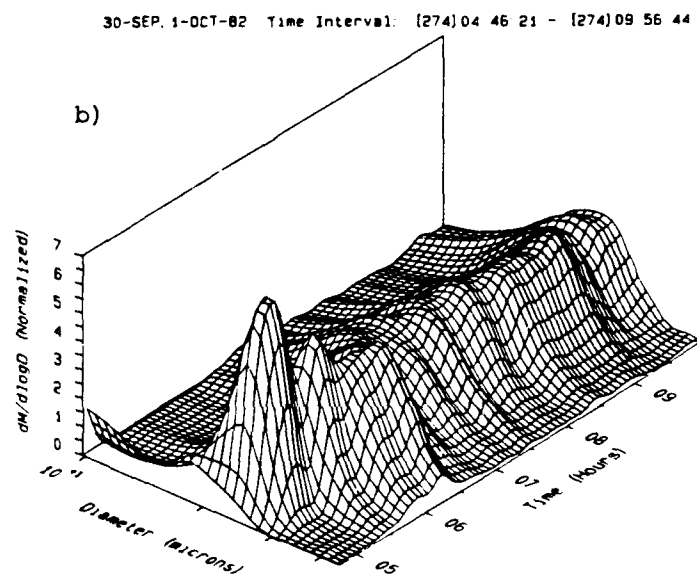
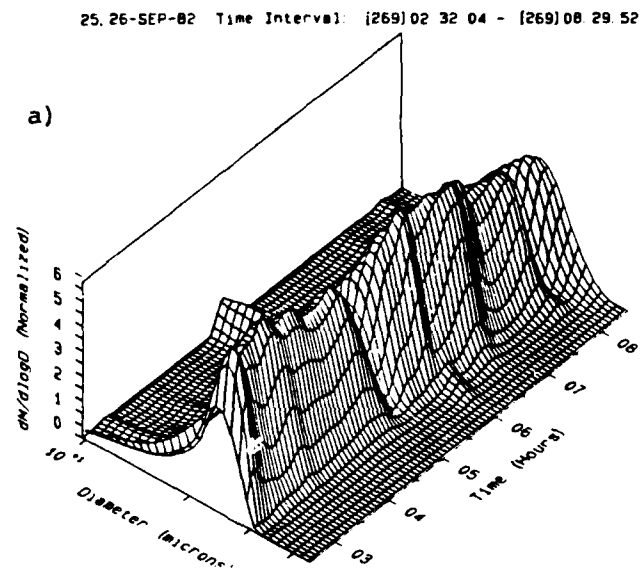


Figure 4.2 (a,b). Normalized fog drop mass distribution versus time during periods of dense fog on a) 25,26 Sept. 1982, b) 30 Sept.-1 Oct. 1982.

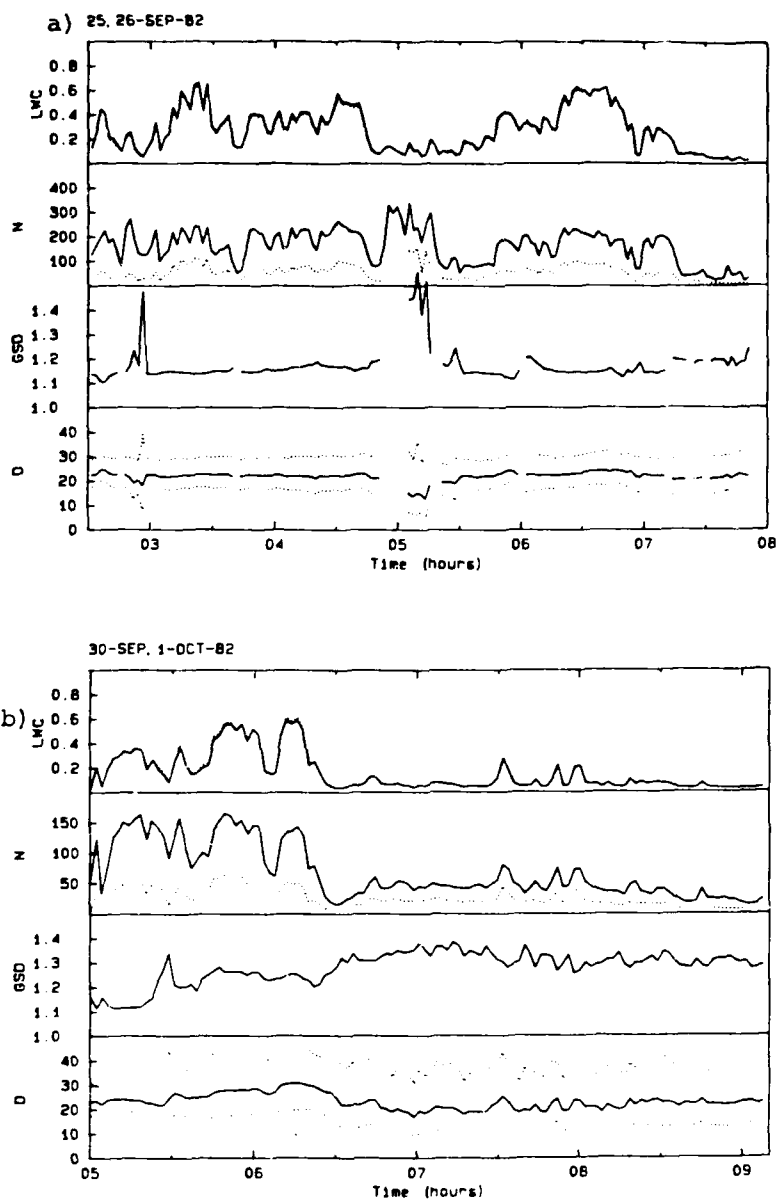


Figure 4.3 (a,b). Drop spectra as measured and derived from a lognormal function fit versus time during periods of dense fog on a) 25,26 Sept. 1982, b) 30 Sept.-1Oct. 1982. Bottom to top respectively, 1) solid - mass median diameter; dotted - 5% and 95% limits of distribution. 2) geometric standard deviation. 3) number concentration: solid - measured; dotted - derived from curve fit. 4) liquid water content: solid - measured; dotted - derived from curve fit.

5.0 Optical Extinction Measurements in Radiation Haze and Fog

5.1 Introduction

Obstruction to vision by the atmospheric aerosol is often represented through a determination of the meteorological visual range. The formula for meteorological visual range can be determined from Koschmieder's Law (Koschmieder, 1924) as follows:

$$B_b = B_h (1 - e^{-b_e V}) , \quad (5.1)$$

where B_b is the apparent brightness (luminance) of a black object at V , B_h the apparent brightness (luminance) of the sky near the horizon at V , b_e the volume optical extinction coefficient (wavelength = 0.55 μm), and V the distance from black object to observer. Koschmieder's Law (Eq. 5.1) can be rearranged to give

$$E = e^{-b_e V} , \quad (5.2)$$

where $E (= [B_h - B_b]/B_h)$ is the threshold contrast of the observer.

For the meteorological visual range, E is considered a constant value of 0.02. By taking the natural logarithm of both sides of Eq. (5.2),

$$V = \frac{3.912}{b_e} . \quad (5.3)$$

Eq. (5.3) is, by definition, the meteorological visual range. Often the terms visibility, standard visibility, meteorological range, meteorological visual range, and visual range are used interchangeably. Henceforth we will use the term "visual range" to imply Eq. (5.3). It should be noted that the visual range defined in this manner depends only upon the volume optical extinction coefficient. For non-absorbing particles (such as water droplets) the volume optical extinction coefficient is identical to the scattering coefficient. The scattering coefficient, b , is defined by

$$b = 2\pi \int_0^\pi B(\phi) \sin\phi \, d\phi, \quad (5.4)$$

where $B(\phi)$ is the intensity of light scattered through angle ϕ by the scatterers in a unit volume per unit flux density of light intercepted by the scatterer. The term "extinction" will be used to represent either of these.

Two common methods of determining the atmospheric extinction in fog and haze are direct measurement employing transmissometers and forward scatter visibility meters, and calculation from measured droplet size spectra. This section is primarily concerned with the application of the AEG-Telefunken MS04 integrating nephelometer (AEG), and Particle Measuring Systems FSSP-100 drop spectrometer (FSSP). Recent field studies by the Atmospheric Science Laboratory (ASL) and the Cloud Physics Section of the Atmospheric Sciences Research Center (ASRC) have involved both instruments operated simultaneously in close proximity to each other. An examination of the data from the two laboratories revealed a bias in the measurements such that the AEG extinction values in clear and haze conditions exceeded the extinction values derived from the FSSP. The opposite trend was observed in fog. Several studies of these instruments have documented measurement problems which explain this observed behavior. Our research goal is to examine the available data and try to explain these relative errors in terms of the measurement environment.

5.2 Data Sources and Instrumentation

We have measured atmospheric extinction as part of an on-going radiation fog research program (Meyer et al., 1986). In all cases the measurements were obtained from the same FSSP drop spectrometer and AEG scattered light meter during the 1981 and 1982 field programs.

Our FSSP is an aspirated probe intended for ground-based operation. In this configuration the sample flow rate ($9.04 \text{ cm}^3 \text{ s}^{-1}$) is a result of the velocity of the particles (26 m s^{-1}) due to the aspirator times the true sampling area (0.348 mm^2). We operated the probe at the 1.5 m level in alternating 20 second samples of A range (2-47 μm diameter, $\Delta D = 3.0 \mu\text{m}$) and D range (0.5-8.0 μm , $\Delta D = 0.5 \mu\text{m}$) during fog to yield data of desired detail. The data were stored as two-minute droplet-size spectra (1 minute A-range, 1 minute D-range). This optical particle counter is described in detail by Knollenberg (1981) and Dye and Baumgardner (1984).

The total extinction may be calculated from the measured drop-size spectrum using the formula,

$$b_e = \sum_{i=1}^{15} \frac{\pi}{4} N_i Q_i D_i^2 , \quad (5.5)$$

where N_i is the number concentration of droplets in the i 'th size bin, D_i the mean diameter of the i 'th bin, and Q_i the mean extinction efficiency within the i 'th bin. The extinction efficiencies were computed using the computer code of Wiscombe (1979). The individual fifteen products within the summation represent the optical extinction-size spectrum when plotted against D_i .

Another measure of the total atmospheric extinction was obtained with the AEG (also at the 1.5 m level). The AEG model MS04 differs from the newer model MS05 only in the method of conversion of the scattered light signal to a visual range value. The MS04 utilizes a servo-balancing system in which a logarithmic grey scale attached to a read out device is positioned to balance the reference and scattered light signal. The MS05 uses a variable range digitally controlled amplifier to obtain the same signal balance. Optically, the instruments are of identical design and the calibration of the MS05 was obtained by direct comparison with the MS04. The only difference in performance is that the MS05 responds immediately to changes in extinction whereas the MS04 value is obtained from the integration over several pulses. The theory for measurements with this type of scattered light meter has been presented by Heintzenberg and Quenzel (1973).

For the AEG the total atmospheric extinction is measured as

$$b = 2\pi \int_{\phi_1}^{\phi_2} B(\phi) \sin\phi \, d\phi , \quad (5.6)$$

where the integration is over the angular range 10° - 120° . The measured scattering coefficient is assumed to be a close approximation of the actual atmospheric scattering coefficient.

5.3 Instrument Performance

5.3.1 FSSP-100

The primary sources of error of the FSSP are in the determination of the sample volume and the particle size thresholds for the pulse height analyzer. Sample volume errors, if present, can be easily handled by rescaling the measured droplet number concentration. Sizing errors are more difficult to manage because the sensitivity depends on the nature of the droplet size distribution.

Several studies of the size calibration of the FSSP have been carried out (Pinnick et al., 1981; Cerni, 1983). The primary conclusions from these studies are:

1. For small aerosols on the order of $0.5\ \mu\text{m}$, the FSSP can be expected to underestimate the number concentration.
2. Based on a comparison of the manufacturer's response curve and the theoretical response curve based on water droplets, it was evident that the instrument response is multi-valued below $4\ \mu\text{m}$ radius and that the use of the manufacturer's calibration will produce somewhat distorted measurements of droplet spectra.
3. Spectral broadening by the FSSP can be expected to lead to overestimates of atmospheric extinction.

At low values of extinction, submicron size particles dominate the extinction spectrum, and the FSSP will underestimate total atmospheric extinction since 1) it tends to underestimate the number concentration of the small aerosols, and 2) the probe is not "seeing" the complete size spectrum, missing particles less than $0.5\ \mu\text{m}$. At some point, when the droplets with the maximum contribution to extinction are large enough to be detected and sized properly by the FSSP, the calculated extinction from the measured droplet spectrum should be in reasonable agreement with observation. As shown by the calibration studies these errors should not exceed 30%.

5.3.2 AEG-MS04

Unlike a transmissometer, which measures the fraction of illumination transmitted over a known path, the AEG measures the light scattered out of a sample volume. Such forward-scattering-type instruments are designed so that the scattered light signal approximates the signal that would be received if the total light scattered from the volume over the angular range from 0 to 180 degrees were intercepted (by definition, the volume optical extinction coefficient, b). However, due to practical considerations, most scattered light meters measure over a truncated angular range (such as 10° - 120° for the AEG). Since particles larger than a few microns scatter light predominantly into a small forward angle, an underestimate of total extinction results from this "angular truncation error". This error

increases with drop size (as does forward scattering) and is most severe in cloud and fog environments.

Several studies of the angular truncation error of forward scattering meters have been conducted (Heintzenberg and Quenzel, 1973; Ensor and Waggoner, 1974; Quenzel et al., 1975; Fitzgerald, 1977). Some of the major findings from these references are:

1. For dry aerosols following a Junge size distribution, small particles ($d \leq 0.1 \mu\text{m}$) contribute little to the angular truncation error and, further, the measurement is relatively insensitive to the index of refraction of the aerosol. The error increases with decreasing slope of the distribution (corresponding to an increase in the large particle concentration).
2. Indicated extinction in cloud and fog environments is underestimated by a factor of 1.4 - 2.0, depending on the size distribution.
3. The extinction ratio (true/measured) is an oscillating function of particle size, with the greatest amplitude change occurring in the haze/fog/cloud droplet range between 1 and $10 \mu\text{m}$ diameter.

Fig. 5.1 shows the complex behavior of the angular truncation factor (the ratio of the measured extinction to true extinction) for the AEG assuming visible light (wavelength = $0.55 \mu\text{m}$) and water drops (real index of refraction = 1.33). As indicated above, the angular truncation error will depend in a complex manner on the exact size distribution of the aerosol present. Because of the oscillating nature of the relative response function, the error expressed as a function of the size, area or volume (mass) characteristic of the aerosol may be multi-valued, but should never be less than about 40% of the true atmospheric extinction.

5.4 Results

An overview of the relative performance of the AEG and FSSP under varying environmental conditions is provided in this section. In addition, we will focus on the behavior of the total and size-spectral extinction coefficient over a range of visual range and temperature conditions during radiation fog. The AEG extinction values were calculated from the measured visual ranges using Eq. (5.3), while corresponding FSSP extinction values were derived from the measured aerosol spectra utilizing Eq. (5.5).

5.4.1 Extinction ratio

Because of the desirability of finding a relationship of the relative error of the AEG and FSSP to some independent parameter, the ratio of extinction from the AEG to extinction calculated from the FSSP data was plotted against liquid water content (LWC) (Fig. 5.2).

The plot includes some 11,000 2-minute observations from the 21 different cases listed in Table 5.1. The data tend to fall into two groups, one corresponding with quasi-clear to haze conditions (the "haze" region [$\text{LWC} < 0.01 \text{ g m}^{-3}$]) and another associated with fog (the "fog" region [$\text{LWC} \geq 0.01 \text{ g m}^{-3}$]). The relatively sparse observations in the zone between fog and haze appear to be related to some natural transition process between the two regions. The extinction ratio is greater than 1.0 in the haze region, but less than 1.0 for the fog observations. This characteristic is related to the size distribution dependence of the error of the AEG and FSSP. At low LWC's, extinction is caused primarily by small droplets which are either undercounted or out of the range of the FSSP. In this region the AEG should be the more accurate instrument. In fogs, associated with higher water contents and larger droplets, the FSSP performs reasonably well, but the AEG suffers from angular truncation error.

Further inspection of the plot of extinction ratio versus LWC in Fig. 5.2 shows a tendency for a somewhat larger scatter in the ratios in the LWC range of 0.01 to 0.1 g m^{-3} . This can be shown to be a direct consequence of the oscillatory nature of the angular truncation factor which was shown in Fig. 5.1. The mean diameter of each spectrum versus LWC is presented in Fig. 5.3. Beyond 0.01 g m^{-3} there is a non-linear increase in mean diameter from about $2 \mu\text{m}$ at 0.01 g m^{-3} to nearly $10 \mu\text{m}$ approaching 1 g m^{-3} LWC. From Fig. 5.1 the angular truncation factor fluctuates rapidly over the diameter range $2 - 10 \mu\text{m}$, while decreasing from a value of about 0.7 to between 0.4 and 0.5. The observed extinction ratios agree remarkably well with the angular truncation factors associated with the fog region data. This supports the theoretical discussion presented earlier, confirming that forward scattering visual range meters need to be corrected for angular truncation error in foggy environments.

In an attempt to quantify the graphical relationship of the extinction ratio versus LWC data, curve fits were derived by the method of least squares. The curve fit parameters for each individual case (individual graphs not shown) are presented in Table 5.1 in categories of ALL data, HAZE ($\text{LWC} < 0.01$) data and FOG ($\text{LWC} \geq 0.01$) data.

5.4.2 Extinction-size spectrum

Ten fog events from the 1981 and 1982 field programs were selected as the data base for this section. These cases comprise over 16 hours of FSSP (A-range) and AEG measurements during radiation fog when the FSSP calculated visual range was less than 1 km. The spectra were averaged for selected categories of visual range and temperature.

5.4.2.1 Visual range categories

Four visual range categories were selected for a variety of reasons. These are A) 0.0 - 0.1 km, B) 0.1 - 0.4 km, C) 0.4 - 1.0 km, and D) 1.0 - 2.0 km. Category A is representative of what we term "severe" fog conditions. The severe fog range falls within the visual range requirements for Category III landing systems at airports. No category III landing systems existed over 10 years ago (Silverman and Weinstein, 1974), and have not recently been placed into routine use. Category B is the "heavy" fog group. Since 1949 the National Weather Service has reported heavy fog for visual range of one-quarter mile or less (Court and Gerston, 1966). Category C has an upper cut-off at 1 km, the accepted visual range threshold of "fog" according to international definition (Huschke, 1959). And finally, Category D represents "thin" fog as prescribed by the International Visibility Code (Hulbert, 1941).

Using Eq. (5.4), the extinction-size spectrum can be calculated for the visual range categories above (Fig. 5.4). These curves have been normalized by the total integrated extinction coefficient and represent the frequency of extinction per micron interval. The severe fog spectrum is peaked around $24\text{ }\mu\text{m}$ with almost all the extinction being accounted for in a narrow region between 10 and $30\text{ }\mu\text{m}$. Nearly 25% of the total extinction results from droplets in the 23-26 μm size bin. As the visual range improves, the extinction spectrum broadens towards smaller drop sizes. The larger drops play a less important role in the degradation of visual range in these lighter fogs.

5.4.2.2 Temperature categories

FSSP drop-size spectra were also averaged for cold ($\leq 0\text{ }^{\circ}\text{C}$) and warm ($> 0\text{ }^{\circ}\text{C}$) temperature conditions for visual ranges of less than or equal to 1 kilometer. An average temperature (1.5 m level) was determined for each two-minute FSSP spectrum in a similar fashion as above.

Fig. 5.5 shows the normalized extinction-size spectra as a function of the two temperature conditions. For both curves the bulk of the contribution to extinction can be attributed to drops in the 10 - $30\text{ }\mu\text{m}$ size range. However, warm fog extinction tends to be influenced by somewhat larger drops. These fogs show a peak in the spectrum in the 23-26 μm bin, whereas the cold fogs peak in the 20-23 μm channel. We have observed that warm fogs tend to be thicker than cold fogs. This may account to some extent for the presence of larger drops through an increase in their residency time.

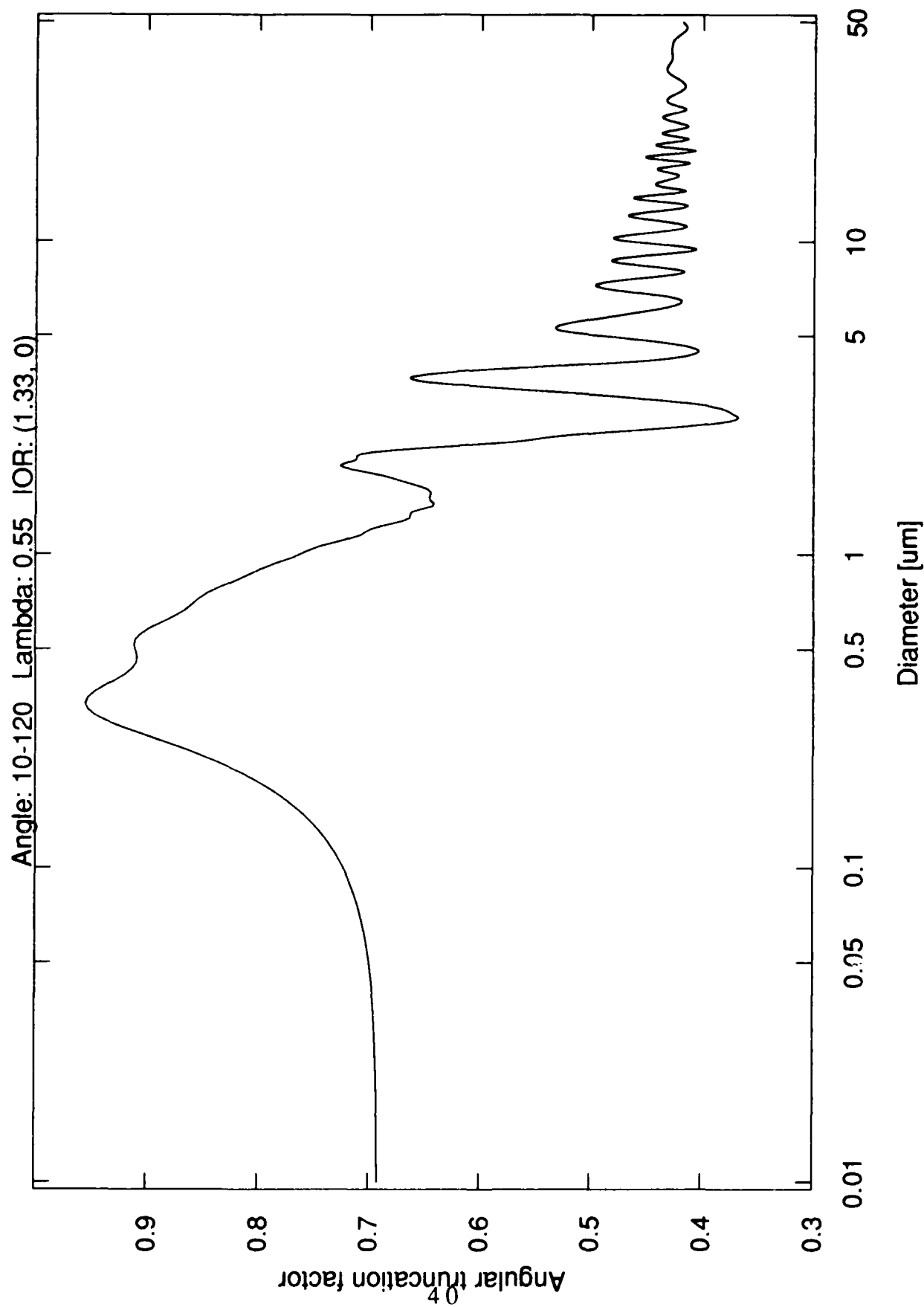


Figure 5.1. Angular truncation factor versus particle diameter for an angular range of 10-120 degrees, wavelength of 0.55 μm , and real index of refraction equal to 1.33.

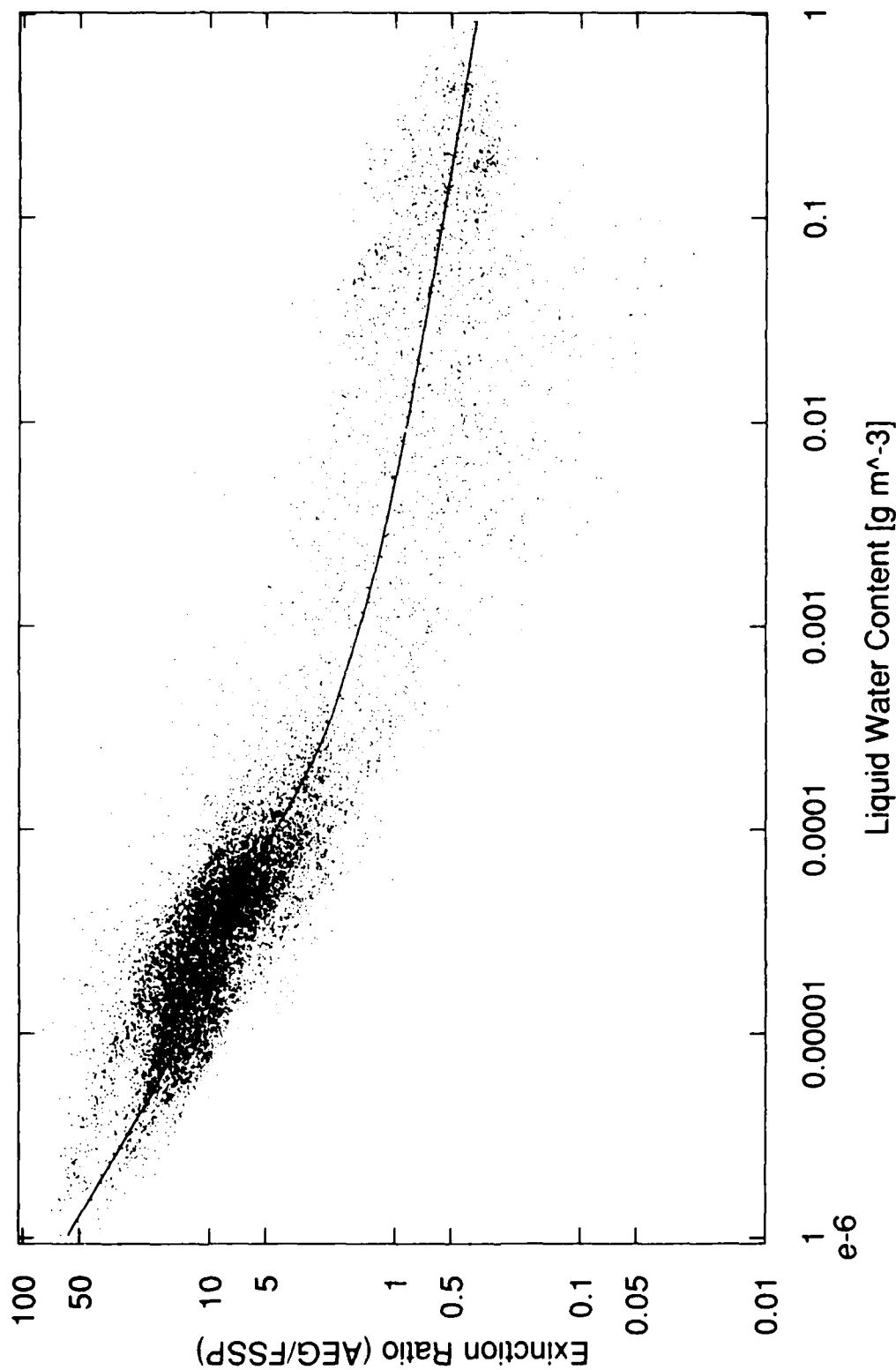


Figure 5.2. Ratio of measure extinction (AEG) to calculated extinction (FSSP) versus liquid water content (FSSP).

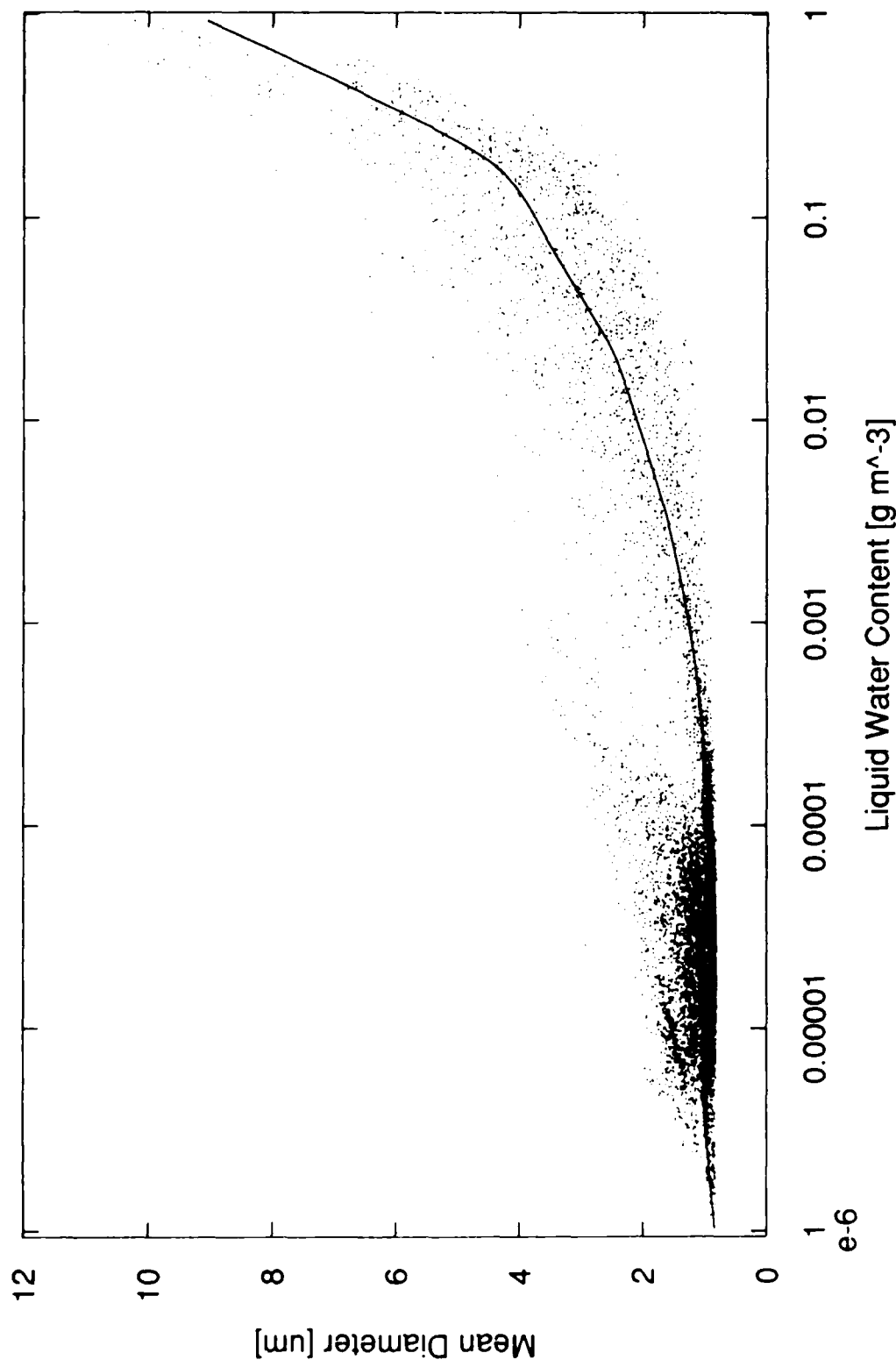


Figure 5.3. Mean diameter of the drop-size distribution versus liquid water content. Both quantities calculated from FSSP data.

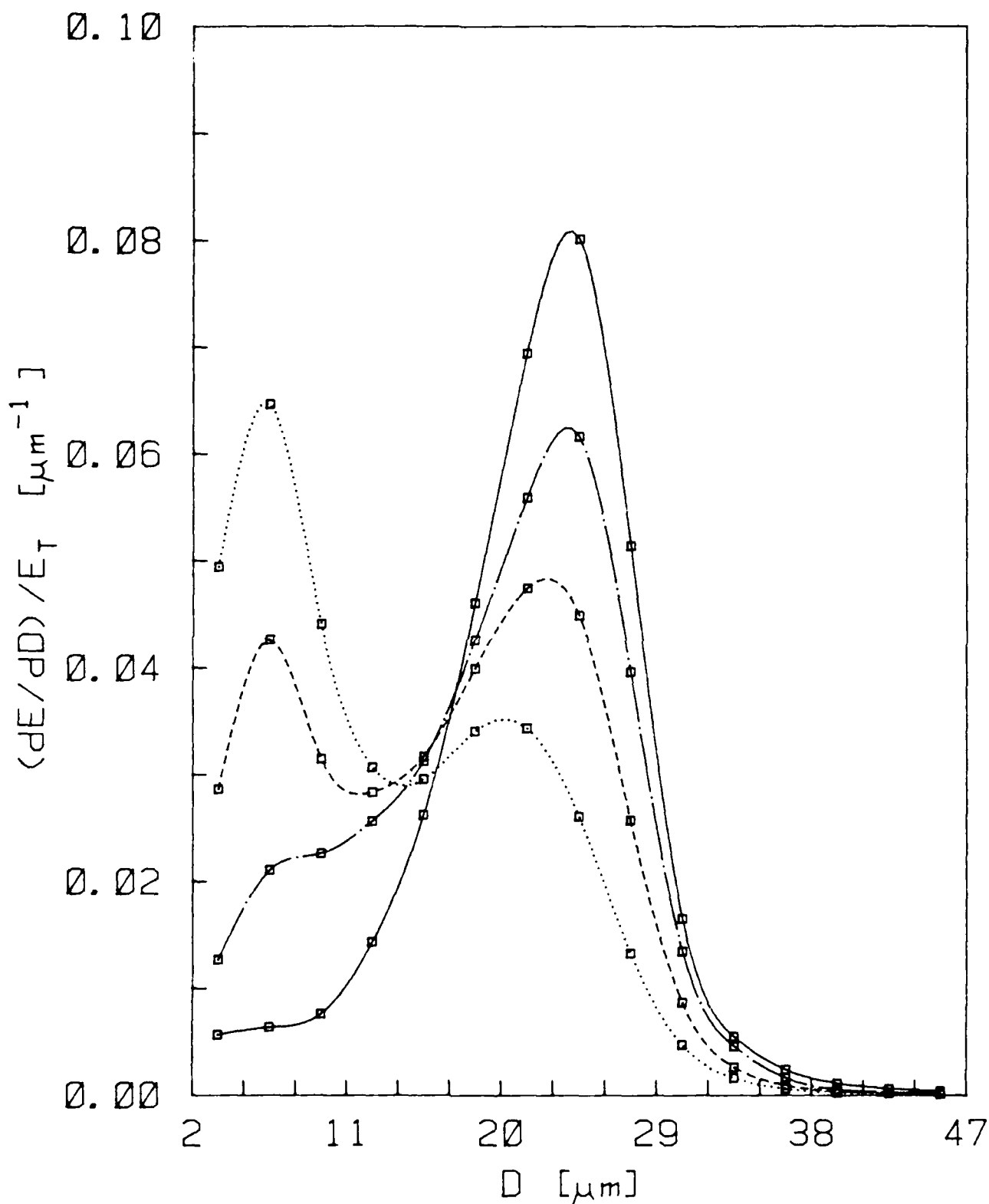


Figure 5.4. Average fog extinction-size spectra for visual range categories A) 0.0-0.1 km (solid), B) 0.1-0.4 km (dot-dash), C) 0.4-1.0 km (dash), and D) 1.0-2.0 km (dot). These curves have been normalized by the total integrated extinction coefficient and represent the frequency of extinction per micron interval.

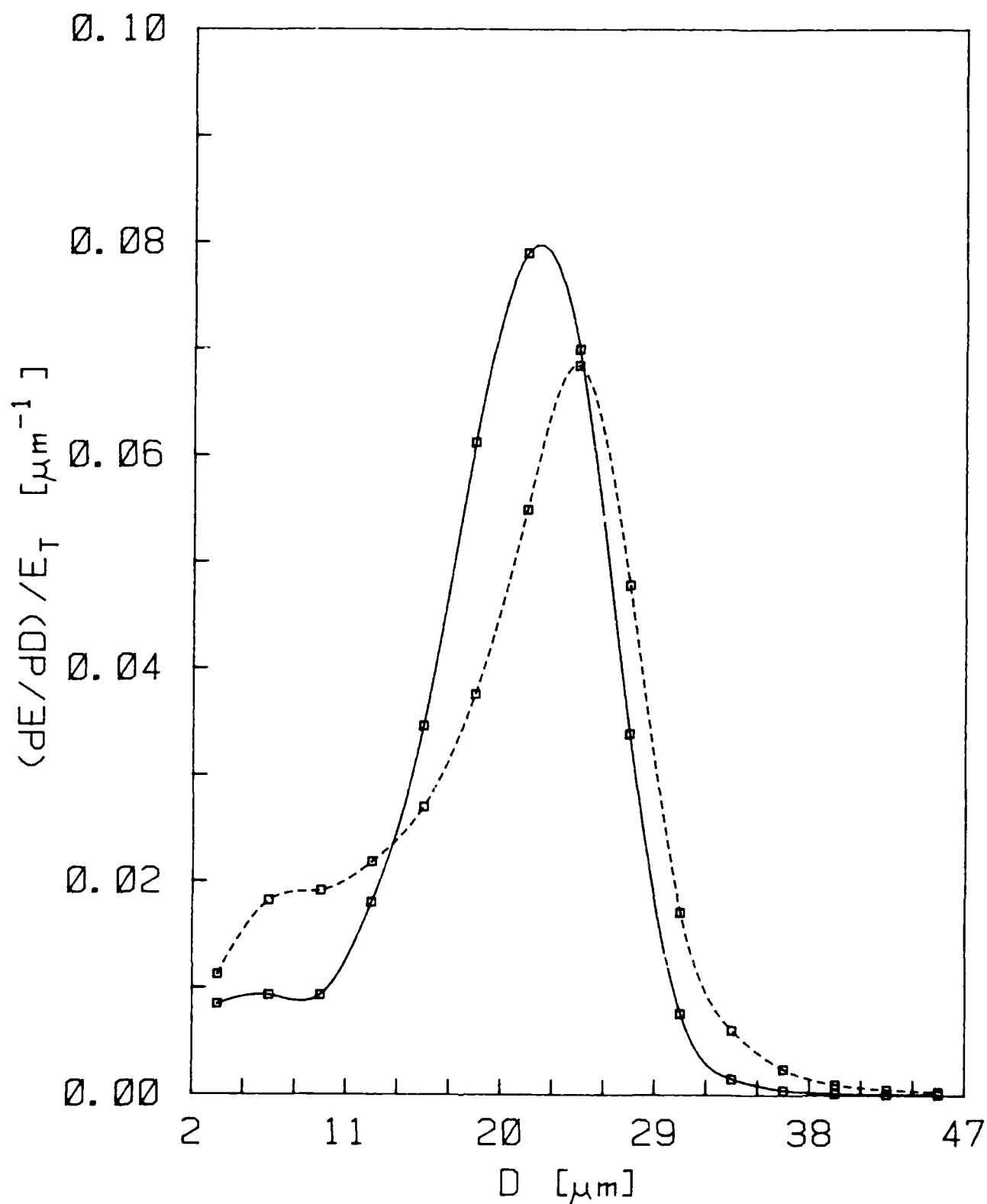


Figure 5.5. Average fog extinction-size spectra for temperature categories 1) $T \leq 0$ C (dash). These curves have been normalized by the total integrated extinction coefficient and represent the frequency of extinction per micron interval.

6.0 Summary

As a result of the program of research conducted under this grant, considerable progress has been made in understanding both fog formation processes and the structure of radiation fog. Some of the more significant findings are:

1) Well defined synoptic scale weather patterns are associated with fog events. Systems most often associated with severe fog events have been identified.

2) The observed seasonal dependence of radiation fog formation has been described by a simple model using standard weather observations. This approach may be applicable to other geographic regions and fog types.

3) The role of initial conditions as precursors to fog formation has emerged as an important consideration. Inclusion of detailed observations in the lower 100 meters of the atmosphere is important to understanding the evolution of a potential fog layer.

4) Radiational cooling of the boundary layer is of primary importance in cooling the boundary layer with turbulent cooling playing a minor role. In cases with significant temperature gradients, advection effects of local winds can be of importance.

5) A common feature of fog cases is the development of a channeled flow along the Hudson valley. Depending on conditions, this flow may act either to promote or retard fog formation.

6) Fog drop spectra in mature fogs have been observed to maintain a nearly constant shape over a period of hours. Shape differences between shallow and deep fogs have been observed with deep fogs being associated with larger drop sizes and broader spectra.

7) Mass distributions of fog drops are well described by the lognormal distribution function. Changes in fog water content are primarily due to variations in drop concentration rather than the width or median drop size.

8) Extinction measurements have been compared with values calculated from drop size spectra with the result that in light fog values from the drop spectrometer are

underestimated while in dense fog the forward scatter meter underestimates extinction due to angular truncation errors. A promising approach seems to be to correct the forward scatter meter based on drop spectra parameters.

These results represent a beginning of the process of understanding the details of fog formation and the structure of radiation fog. Because of the tremendous information content of the data set, we expect that other important processes will be resolved as work continues. An important goal of this effort has been to try to integrate the results into a coherent picture of fog processes. Perhaps one of the most important results of this study is the establishment of a firm basis for the formulation of future field studies of radiation fog.

7.0 References

- Baroniti, P., and S. Elweig, 1973: A study of droplet spectra in fogs. J. Atmos. Sci., **30**, 903-908.
- Baumgardner, D., 1983: An analysis and comparison of five water droplet measuring instruments. J. Appl. Meteor., **22**, 891-910.
- Brunt, D., 1952: Physical and Dynamical Meteorology. Cambridge University Press, London, 428 pp.
- Byers, H. R., 1959: General Meteorology. McGraw-Hill, 481 pp.
- Cerni, T. A., 1983: Determination of the size and concentration of cloud drops with an FSSP. J. Appl. Meteor., **22**, 1346-1355.
- Corradini, C., and G. Tonna, 1979: On the reliability of the parameterizations of microphysics in fog models. J. Appl. Meteor., **18**, 487-494.
- Corradini, C., and G. Tonna, 1980: The parameterization of the gravitational water flux in fog models. J. Appl. Meteor., **37**, 2535-2539.
- Court, A., and R. D. Gerston, 1966: Fog frequency in the United States. The Geographic Review, **56**, 543-550.
- Dye, J. E., and D. Baumgardner, 1984: Evaluation of the forward scattering spectrometer probe. Part I: Electronic and optical studies. J. Atmos. Oceanic Technol., **1**, 329-344.
- Eldridge, R. G., 1971: The relationship between visibility and liquid water content in fogs. J. Atmos. Sci., **28**, 1183-1186.
- Emmons, G., and R. B. Montgomery, 1947: A note on the physics of fog formation. J. Meteor., **4**, 206.
- Ensor, D. S., and A. P. Waggoner, 1974: Angular truncation error in the integrating nephelometer. Atmos. Environ., **4**, 481-487.
- Fitzgerald, J. W., 1977: Angular truncation error of the integrating nephelometer in the fog droplet size range. J. Appl. Meteor., **16**, 198-204.
- Forkel, R., U. Sievers, and W. Zdunkowski, 1987: Fog modeling with a new treatment of the chemical equilibrium condition. Beitr. Phys. Atmos., **60**, 340-360.
- George, J. J., 1940: Fog: Its causes and forecasting with special reference to eastern and southern United States. Bull. Amer. Meteor. Soc., **21**, 135-148.
- George, J. J., 1951: Fog. in Compendium of Meteorology. American Meteorological Society, Boston, 1334 pp.

- Gross, G. and F. Wipperman, 1987: Channeling and countercurrent in the upper Rhine valley: Numerical simulations. J. Climate and Appl. Meteor., **26**, 1293-1304.
- Hardwick, W. C., 1973: Monthly fog frequency in the continental United States. Mon. Wea. Rev., **101**, 763-766.
- Heintzenberg, J., and H. Quenzel, 1973: Calculations on the determination of the scattering coefficient of turbid air with integrating nephelometers. Atmos. Env., **7**, 509-519.
- Hulbert, E. O., 1941: Optics of atmospheric haze. J. Opt. Soc. Am., **31**, 467-476.
- Huschke, R. E., 1959: Glossary of Meteorology. American Meteorological Society. 638 pp.
- Jiusto, J. E., 1981: Fog structure. in Clouds, Their Formation, Optical Properties, and Effect, P. V. Hobbs and A. Deepak, Eds., Academic Press, 495 pp.
- Knollenberg, R. G., 1981: Techniques for probing cloud microstructure. in Clouds, Their Formation, Optical Properties, and Effect, P. V. Hobbs and A. Deepak, Eds., Academic Press, 495 pp.
- Koschmieder, H., 1924: Theorie der horizontalen Sichtweite. Beitr. Phys. d. freien Atmos., **12**, 33-55 and 171-181.
- Kunkel, B. A., 1982: Microphysical properties of fog at Otis AFB. AFGL-TR-82-0026, Air Force Geophysical Laboratory, Hanscom AFB, MA.
- Kunkel, B. A., 1984: Parameterization of droplet terminal velocity and extinction coefficient in fog models. J. Climate and Appl. Meteor., **23**, 34-41.
- Lala, G. G., L. Dzamba, and M. B. Meyer, 1986: Activated particle and droplet spectra in radiation fog. Proc. Conf. on Cloud Physics, Sept. 22-26, 1986, Snowmass, Co.,
- Low, R. D. H., 1979: A theoretical investigation of cloud/fog extinction coefficients and their spectral correlations. Contr. to Atmos. Physics, **52**, 44-57.
- Mason, J., 1982: The physics of radiation fog. J. Meteor. Soc. Japan, **60**, 486-498.
- Meyer, M. B., and J. E. Jiusto, 1982: Radiation-fog intensities associated with surface synoptic patterns at Albany, New York. Proc. 9th Conf. on Weather Forecasting and Analysis, June 28 - July 1, 1982, Seattle WA, AMS.
- Meyer, M. B., J. E. Jiusto, and G. G. Lala, 1986: FOG-82: A cooperative field study of radiation fog. Bull. Amer. Meteor. Soc., **67**, 825-832.
- Musson-Genon, L., 1987: Numerical simulation of a fog event with a one-dimensional boundary layer model. Mon. Wea. Rev., **115**, 529-607.
- Oliver, D. A., W. S. Lewellen, and G. G. Williamson, 1978: The interaction of turbulent and radiative transport in the development of fog and low-level stratus. J. Atmos. Sci., **35**, 301-316.

- Peace, R. L., 1969: Heavy-fog regions in the conterminous United States. Mon. Wea. Rev., 97, 116-123.
- Pilié, R. J., E. J. Mack, W. C. Kocmond, W. J. Eadie, and C. W. Rogers, 1975: The life cycle of valley fog. Part II: fog microphysics. J. Appl. Meteor., 14, 364-374.
- Pinnick, R. G., D. M. Garvey, and L. D. Duncan, 1981: Calibration of Knollenberg FSSP light-scattering counters for measurement of cloud droplets. J. Appl. Meteor., 20, 1049-1057.
- Quenzel, H., G. H. Ruppersberg, and R. Schellhase, 1975: Calculations about the systematic error of visibility-meters measuring scattered light. Atmos. Environ., 9, 587-601.
- Roach, W. T., R. Brown, S. J. Caughey, J. A. Garland, and C. J. Readings, 1976: The physics of radiation fog: I - a field study. Quart. J. Roy. Meteorol. Soc., 102, 313-333.
- Rhode, B., 1962: The effect of turbulence on fog formation. Tellus, 14, 49-86.
- Silverman, B. A., and A. I. Weinstein, 1974: Fog. Chapter 9, in Weather and Climate Modification (Ed. W. N. Hess), John Wiley and Sons, 842 pp.
- Stone, R. G., 1936: Fog in the United States and adjacent regions. Geogr. Rev., 26, 111-134.
- Tampieri, F., and C. Tomasi, 1975: Size distribution models of fog and cloud droplets in terms of the modified gamma function. Tellus, 28, 103-117.
- Taylor, G. I., 1917: The formation of fog and mist. Quart. J. R. Met. Soc., 43, 241-268.
- Turton, J. D., and R. Brown, 1987: A comparison of a numerical model of radiation fog with detailed observations. Quart. J. R. Met. Soc., 113, 37-54.
- Welch, R. M., and M. G. Ravichandran, 1986: Prediction of quasi-periodic oscillations in radiation fogs. Part I: Comparison of simple similarity approaches. J. Atmos. Sci., 43, 633-651.
- Willett, H. C., 1928: Fog and haze, their causes, distribution, and forecasting. Mon. Wea. Rev., 56, 435-468.
- Willett, H. C., 1944: Descriptive Meteorology. Academic Press, New York, 310 pp.
- Wiscombe, W. J., 1979: Mie scattering calculations: advances in technique and fast, vector-speed computer codes. NCAR Tech. Note TN-140+STR, 62 pp.

8.0 Publication Summary

Meyer, M.B., G.G. Lala and D.R. Fitzjarrald, 1985: Tethered balloon soundings during radiation fog evolution. Proc. 2nd Intl. Conf. on the Aviation Weather System, AMS, June 19-21, 1985, Montreal, P.Q., Canada.

Lala, G.G., and M.B. Meyer, 1985: The uncertainty of visibility measurements in radiation fog. Proc. 2nd Intl. Conf. on the Aviation Weather System, AMS, June 19-21, 1985, Montreal, P.Q., Canada.

Lala, G.G., L. Dzamba and M.B. Meyer, 1986: Activated particle and droplet spectra in radiation fog. Proc. 23rd Conf. on Radar Meteorology and the Conf. on Cloud Physics, AMS, Sept. 22-26, 1986, Snowmass, CO.

Meyer, M.B. and G.G. Lala, 1986: The optical extinction-size spectrum in radiation fog. Proc. 23rd Conf. on Radar Meteorology and the Conf. on Cloud Physics, AMS, Sept. 22-26, 1986, Snowmass, CO.

Fitzjarrald, D.R. and G.G. Lala, 1986: Observed fine structure in radiation fog. Proc. 23rd Conf. on Radar Meteorology and the Conf. on Cloud Physics, AMS, Sept. 22-26, 1986, Snowmass, CO.

Meyer, M.B., G.G. Lala and J.E. Jiusto, 1986: Fog-82: A cooperative field study of radiation fog. Bull. Amer. Meteor. Soc., 67, 825-832.

Lala, G.G., 1987: Radiation fog: Characteristics and formation processes. Proc. 25th AIAA Aerospace Sciences Meeting, Jan. 12-15, 1987, Reno, NV.

9.0 Scientific Personnel

1. Michael B. Meyer, Research Associate
2. Kurt Kebschull, Research Assistant
3. Len Dzamba, Research Assistant
4. Ann Starr, Research Assistant
5. John Sicker, Technical Specialist
6. Hye Joo You, Graduate Student
7. Carol Hsu, Graduate Student
Masters Thesis: Surface Heat and Moisture Budgets
8. M.B. Meyer, Graduate Student
Dissertation Title: The character of the extinction-size spectrum during radiation fog life-cycles.
9. J. Miller, Graduate Student
Thesis Subject: Aerosol processes in radiation fog.

END

DATE

FILMED

5-88

DTIC